doi: 10.1093/pasj/xxx000

arXiv:2105.09449v1 [astro-ph.GA] 20 May 2021

Hot Molecular Core Candidates in the Galactic Center 50 km s^{-1} Molecular Cloud

Ryosuke Miyawaki[1], Masato Tsuboi[2,3], Kenta Uehara[3], and Atsushi Miyazaki[4]

[1]College of Arts and Sciences, J.F. Oberlin University, Machida, Tokyo 194-0294, Japan
[2]Institute of Space and Astronautical Science, Japan Aerospace Exploration Agency, 3-1-1 Yoshinodai, Chuo-ku, Sagamihara, Kanagawa 252-5210, Japan
[3]Department of Astronomy, The University of Tokyo, Bunkyo, Tokyo 113-0033, Japan
[4]Japan Space Forum, Kanda-surugadai, Chiyoda-ku,Tokyo,101-0062, Japan

*E-mail: miyawaki@obirin.ac.jp

Received ⟨Octorber–5–2020⟩; Accepted ⟨May–19–2021⟩

Abstract

We present the results based on the 2.″5-resolution observations using Atacama Large Millimeter/Submillmeter Array (ALMA) of the Galactic Center Molecular Cloud G−0.02−0.07, or the 50 km s^{-1} Molecular Cloud (50 MC), in the SO (N_J=2_2-1_1) line and 86-GHz continuum emission, the combination of which is considered to trace "hot molecular core candidates" (HMCCs) appearing in the early stage of massive-star formation. In the 86-GHz continuum image, we identified nine dust cores in the central part of the 50 MC, in which four famous compact HII regions are located. No new ultra-compact HII regions were found. We also identified 28 HMCCs in the 50 MC with the SO line. The overall SO distribution had no clear positional correlation with the identified HII regions. The HMCCs in the 50 MC showed a variety of association and non-association with dust and Class-I CH_3OH maser emissions. The variety suggests that they are not in a single evolutionary stage or environment. Nevertheless, the masses of the identified HMCCs were found to be well approximated by a single power law of their radii, $M_{\rm LTE}/(M_\odot)$=5.44 $\times 10^5$ (r/(pc))$^{2.17}$ at $T_{\rm ex}$ = 50–100 K. The derived HMCC masses were larger than those of the molecular cores with the same radii in the 50 MC and also than those of the molecular clumps in the Galactic disk. Additional observations are needed to confirm the nature of these HMCCs in the 50 MC.

Key words: Galaxy: center, ISM: clouds, ISM: individual (G-0.02-0.07, 50 km s^{-1} Molecular Cloud), stars: massive, formation, radio lines: ISM

1 INTRODUCTION

The Galactic Center 50 km s^{-1} Molecular Cloud (50 MC) is located only 3′ from Sagittarius A* (Sgr A*) in the Central Molecular Zone (CMZ) (Morris & Serabyn 1996). The hot and turbulent medium of the 50 MC is believed to have been generated by a strong tidal field, cloud-cloud collisions (CCCs), stellar winds, supernova shocks (Morris & Serabyn 1996).

In the CMZ, a very steep power-law linewidth-size relation of N_2H^+ molecule has been observed down to 0.1 pc scale, which is likely to originate in the decay of supersonic gas motion in strong shocks (Kauffmann et al. 2017a). In such environment, star formation in the CMZ clouds may be suppressed (Kauffmann et al. 2017a). Many CMZ molecular clouds have also been observed to have unusually shallow density gradients (and corresponding steep mass-size relations) compared with most regions elsewhere in the Milky Way (Kauffmann et al. 2017b). Lu et al. (2019a) argued that the star formation in the CMZ clouds is inactive overall. The dense gas fractions of the other observed clouds except Sgr C are smaller than 1 % and the star formation rate (SFR) is similarly low (Lu et al. 2019a). They also suggested that the low SFR in the CMZ could be be-

© 2021. Astronomical Society of Japan.

cause there is less gas confined in gravitationally bound cores (Lu et al. 2019a, 2019b). The cores may be prevented from gravitationally collapses by the strong turbulence in this region or if it started it may have only recently started. The extreme environment in the CMZ provides unique opportunities for studying star formation in the centers of external galaxies in general.

The 50 MC has a string of three compact HII regions (CHII) and one ultra-compact HII region (UCHII) in G−0.02−0.07, or Sgr A East A–D (e.g. Ekers et al. 1983; Goss et al. 1985; Yusef-Zadeh et al. 2010; Mills et al. 2011). The HII regions appear to lie along a dense ridge of the 50 MC, the "molecular ridge" by Coil & Ho (2000). The HII regions, Sgr A East A–D (hereafter we refer to them as HII-A, HII-B, HII-C, and HII-D as in Tsuboi et al. (2019), respectively, are thought to host a single late O-type or early B-type star for each and to be at the age of $\sim 10^4$ years, with HII-D being the youngest given its small nebular size (Yusef-Zadeh et al. 2010; Mills et al. 2011; Tsuboi et al. 2019).

The CMZ molecular clouds are known to contain strong shock waves (e.g. Tsuboi et al. 2012), which are responsible to generate filamentary structures often observed in the Galactic disk clouds (Rathborne et al. 2014, 2015; Bally et al. 2014). Similar filamentary structures have been found in the 50 MC (Uehara et al. 2017) and G0.253+0.016 (Rathborne et al. 2015).

Uehara et al. (2017, 2021) identified 27 molecular-cloud filaments in the 50 MC and suggested that filaments are ubiquitous also in the molecular clouds in the CMZ (André et al. 2010). Furthermore, Uehara et al. (2019) showed that the cloud-cloud collision (CCC) efficiently formed massive bound cores even if the slope of the core mass function (CMF) was not greatly altered by CCC. Active star formation is expected to occur in these cold (∼20 K) cores, including those that created the above-mentioned three CHIIs and one UCHII. The cores will then collapse and evolve to warm (∼100 K) hot molecular cores (HMCs).

In the standard evolutionary scenario of massive stars, high-mass starless cores (HMSCs) represent the earliest evolutionary stage of massive star formation (Motte et al. 2018). In the next stage, high-mass protostellar objects (HMPOs) form in the HMSCs and the HMSCs evolve to HMCs. In the Galactic disk, HMCs have been observed in many molecular emission lines from millimeter to submillimeter wavelengths. The HMC has diameters ≤ 0.1 pc, densities $\geq 10^7$ cm^{-3}, and temperatures $\geq$ 100 K. The lifetimes of HMCs are 10^4–10^5 yr (Herbst & van Dishoeck 2009; Battersby et al. 2017). The HMC is considered to represent the evolutionary stage in a massive star formation in which protostars grow through active accretion of circumstellar material (e.g. Kurtz et al. 2000; Beuther et al. 2007). Observations with a high angular resolution suggest that some HMCs are heated by embedded sources, which are usually suspected to be HMPOs or massive young stellar objects (MYSOs) (e.g. Rolffs et al. 2011; Jiménez-Serra et al. 2012; Sanna et al. 2014; Silva et al. 2017). As a result, HMPOs produce strong millimeter continuum and mid-infrared emission but no detectable centimeter emission (Sridharan et al. 2002). Since the centimeter emission is free-free emission from ionized gas, no significant centimeter emission implies that HMPOs have not yet reached the stage in which they produce Lyc photons and ionize the surrounding material. Subsequently, a central massive protostar comes to produce a large quantity of ionizing radiation and to form a hyper-compact HII region (HCHII), which evolves to an HII region after UCHII and CHII (De Pree et al. 2004).

Here we focus on the evolutionary stage between the massive molecular cores and UCHIIs. It is important for understanding of the early stage of massive star formation in the CMZ to look for the objects between the HMSC and UCHII stages.

In this paper, we describe the radio continuum and spectral line observations of the 50 MC and data reduction in § 2. We show the observational results and identify Hot Molecular Core Candidates (HMCCs) in the cloud in § 3. We discuss results from the continuum and the SO, HC^{15}N, and CH_3OH data and discuss the role of the HMC in the early stage of massive star formation in the CMZ in § 4.

2 OBSERVATIONS AND DATA REDUCTION

The observations of SO ($N_J = 2_2 - 1_1$ at 86.09355 GHz), ^{34}SO ($N_J = 2_3 - 1_2$ at 97.71540 GHz and $N_J = 5_4 - 4_4$ at 96.78176 GHz), HC^{15}N (J=1−0 at 86.05497 GHz), CH_3OH ($J_{K_a,K_c}=2_{1,1}-1_{1,0}$ E at 96.75551 GHz), and H42α at 85.68818 GHz were made as a part of the Atacama Large Millimeter/Submillmeter Array (ALMA) Cy 1 wide-field observation (2012.1.00080.S. PI M.Tsuboi). The observation consisted of a 136-pointing mosaic with the 12-m array and a 68-pointing mosaic with the 7m array (ACA), covering a total of 330″ × 330″ area including both the 50 MC and Sgr A*.

The frequency channel width was 244 kHz, corresponding to the velocity resolution of 1.7 km s^{-1} (488 kHz). The objects J0006−0623, J1517−2422, J717−3342, J1733−1304, J1743−3058, J1744−3116, and J2148+0657 were used as the phase calibrators. The flux density scale was determined using Titan, Neptune, and Mars. We reduced the data using the standard packages of CASA (McMullin et al. 2007). The line emissions were separated from the continuum emission in the UV data using the CASA task UVCONTSUB. For the line emissions, the UV data for each channel was CLEANed and Fourier-transformed to a map, and all the resultant maps were combined to three-dimensional data cubes in the right-ascension, declination, and frequency space. The final images were made by applying natural weighting for the visibility (UV) data to obtain a better signal-to-noise ratio. The resultant synthesized beam

size was $2\farcs49 \times 1\farcs85$ (PA=$-89\fdg70$) for the continuum and SO, ^{34}SO, and HC^{15}N spectral line images. The CH_3OH lines were detected in the other sideband. The synthesized beam size of the CH_3OH maps was $2\farcs30 \times 1\farcs66$ (PA=$-86\fdg39$). The typical 3σ rms noise level was 1.0 mJy beam^{-1}, or 35.4 mK, in all the maps. The line profiles of a channel were integrated over 2 km s^{-1} at both bands.

We adopt 8.5 kpc as the distance to the Galactic center; $24''$ corresponds to about 1 pc at the distance, and thus our beam size corresponds to about 0.1 pc. The field center was α(J2000)=$17^{\rm h}45^{\rm m}52\fs0$, δ(J2000)=$-28^\circ59'30\farcs0$.

3 RESULTS AND HMCC IDENTIFICATION

3.1 86 GHz Continuum Emission

Figure1 shows the 86-GHz continuum image of the 50 MC region (see also Figure 1 in Tsuboi et al. (2019)). Although a 96-GHz continuum image was obtained simultaneously, we do not use it in this continuum analysis because it is essentially the same as the 86-GHz image, which alone provides the sufficient sensitivity. The sources HII-A, HII-B, HII-C, and HII-D (sources A, B, C, and D), which are prominent in the centimeter continuum maps (Mills et al. 2011), are also prominent in the 86-GHz continuum image. The known centimeter-continuum faint sources in the region, G0.008−0.07 (sources E and F) and G−0.04−0.12 (e.g. Mills et al. 2011), are also clearly detected.

Although the millimeter continuum emission is considered to mainly originate from ionized gas through the free-free emission mechanism, a possibility of non-thermal origin characteristic in the Galactic center, e.g., emission related with Sgr A*, is not totally excluded. A reliable probe to distinguish the thermal and non-thermal origins is hydrogen recombination lines; if they are detected, the millimeter continuum emission from the source is likely to be in thermal origin. In this case, one of the hydrogen recombination lines, the H42α line, has been detected toward HIIs A–D, G0.008−0.07, and G−0.04−0.12 (e.g. Mills et al. 2011; Tsuboi et al. 2019). Therefore, their emission is likely to be in thermal origin. Figure 2 shows the distributions of the 86-GHz continuum and H42α line emissions. Although nine dust cores are detected in the 86-GHz continuum emission (sources a–i in Figure 2 Left panel; n.b., these sources are not detected in the H42α recombination line in Figure 2 Right panel). A similar situation has been also reported in M0.014−0.054 (Tsuboi et al. 2021). In addition, Walker et al. (2018) have detected massive dust cores, which will eventually grow to HCHIIs, in the CMZ's dust ridge.

Source a corresponds to the HC^{15}N core located $45''$ northeast of "Northern Ridge", which will be discussed in section 3.4.1. Sources b, c, e, h, and i are associated with HMCCs as mentioned later. Sources d, f, and g have no corresponding HMCCs.

By contrast, source j is detected also in the H42α recombination line (see the right panel of Figure 2). Hence, source j should have ionized gas and be regarded as a HCHII candidate. Table 1 lists these sources.

Figure 3 shows the H42α recombination-line spectra toward HII-D and source j. The spectrum toward HII-D has a single peak at around the LSR velocity of 50 km s^{-1}. The spectrum toward source j also has a marginal peak at around the LSR velocity of 50 km s^{-1}. The blue curve in the figure shows the 11-ch running mean of the spectrum. The peak is identified in the mean spectrum. The radio recombination lines from the HCHIIs are known to be extremely broad, typically ΔV =40–50 km s^{-1} and sometimes greater than 100 km s^{-1}(e.g. Sewilo et al. 2004, 2011), and the width tends to be broader at lower-frequency transitions. However, the observed velocity width of the H42α recombination line of source j is only 30 km s^{-1}, which is greatly narrower than those of typical HCHIIs. In addition, the location of source j is adjacent to HII A. Therefore, we conclude that source j is a part of the shell-like structure of HII-A.

If the UCHIIs and HCHIIs exist in the 50 MC, their flux densities are expected to be 200–700 mJy on the basis of the typical flux density of the HCHIIs observed in the Galactic disk at 43 GHz (Sewilo et al. 2011). The observed flux densities of HII A–D at 86 GHz were 426, 141, 172, and 90 mJy, respectively (Tsuboi et al. 2019). Combining with the facts that their continuum emissions at 86 GHz are optically thin and have flat spectrum indexes (~-0.1) because they are free-free emission, we should be able to detect them at a similar intensity if the UCHIIs and HCHIIs exist in the 50 MC. However, we detected none. Therefore, we conclude that no new UCHIIs or HCHIIs exist in this region.

3.2 Molecular Line Emission as HMC Tracers

The HMC is generally characterized by a high gas temperature exceeding 100 K and rich chemistry observable in molecular emission lines in mm and sub-mm wavelengths. Molecular emission lines such as SO, SO_2, CH_3OH, and CH_3CN are often detected in the spectra of HMCs. In the 50 MC, the SO ($N_J = 2_2$ - 1_1) emission line is clearly detected in spectra of the HMCCs. We find that although the $N_J = 2_3$ - 1_2 emission line of ^{34}SO is also detected, the highly excited $N_J = 5_4$ - 4_4 emission line is not detected with a significance of 3σ. Then, we further analyze the SO molecular line in order to obtain the spatial and velocity distributions of the molecular gas in the HMCCs.

The CH_3OH lines can also be used as tracers of HMCs. We detected six lines of CH_3OH in the field of the 50 MC; among them, we here focus on J_{K_a,K_c}=$2_{1,1}$-$1_{1,0}$ A^{--} at 96.75828 GHz, which is not blended with other lines above the 3σ noise

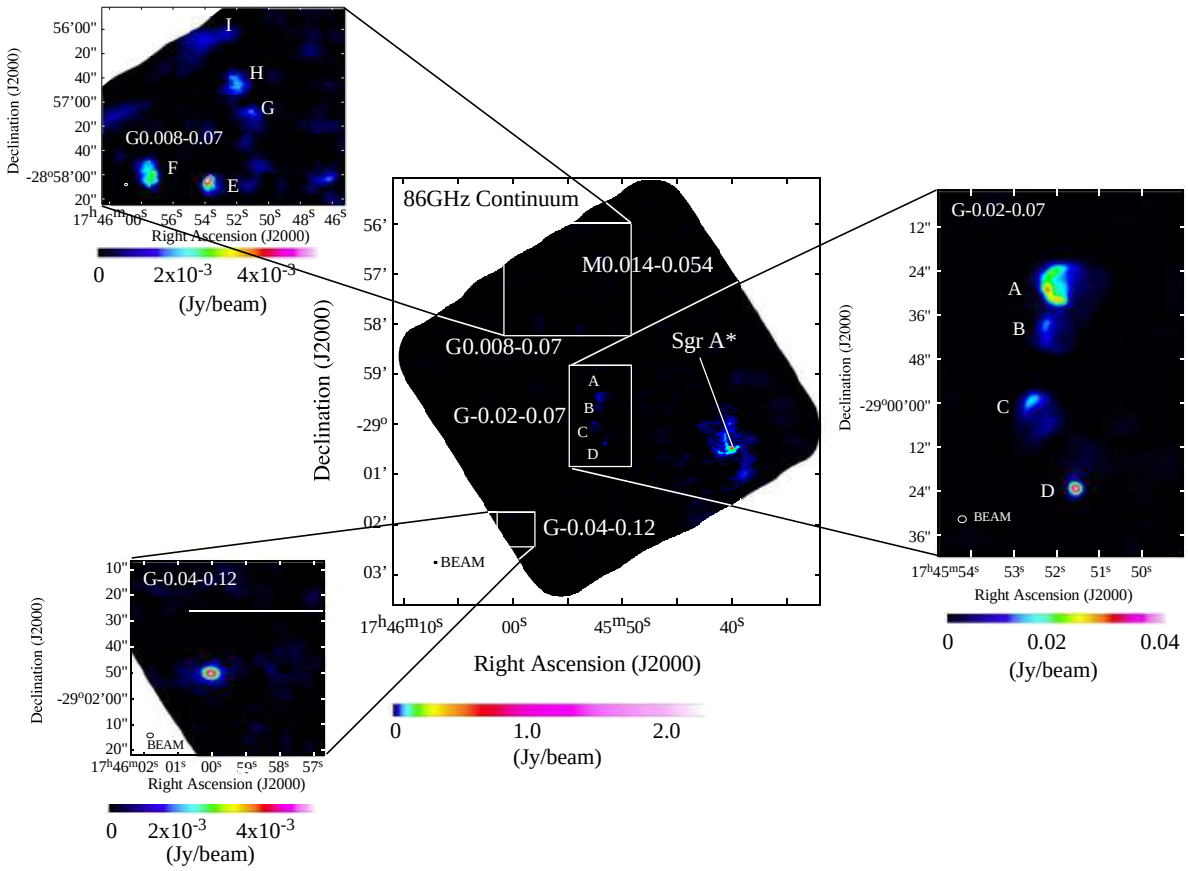

Fig. 1. (Center) 86-GHz continuum map of the observed area, together with the zoomed-up maps for the selected 3 locations: (Right) 8.4-GHz sources A, B, C, and D (Mills et al. 2011), (Upper left) G0.008−0.07, (Lower left) G−0.04−0.12. The intensity scale is indicated in the color bar below each panel. The angular resolution is 2.″49×1.″85 (PA=−89.°70). The beam size is indicated at the bottom left corner of each panel.

Table 1. Hot Molecular Core Candidates in the 50 MC selected on the basis of the 86-GHz continuum and H42α line emissions

86GHz	Position		Size	Flux	Gas Mass	Gas Mass	Mean number	Mean number	Note
Continuum	Right Ascension	Declination	Max × Min		T_d=50K	T_d=100K	density T_d=50K	density T_d=100K	
#	J(2000)	J(2000)	arcsec (″)	(mJy)	M_{dust} ($M_\odot$)	M_{dust} ($M_\odot$)	(cm^{-3})	(cm^{-3})	
a	$17^h45^m46^s.29$	-28°58′03.″32	6.16 × 3.23	2.92	3.52×10^2	1.80×10^2	1.43×10^6	7.31×10^5	north of North Ridge
b	$17^h45^m52^s.12$	-28°58′53.″63	15.39 × 5.16	4.52	5.45×10^3	2.78×10^3	2.78×10^6	1.42×10^6	HMC02, C1P1,C1P2 (Lu et al. 2019a)
c	$17^h45^m49^s.39$	-28°58′53.″39	6.25 × 4.49	7,26	8.76×10^2	4.47×10^2	2.13×10^6	1.09×10^6	HMC05
d	$17^h45^m58^s.24$	-28°59′12.″75	9.83 × 3.98	5.55	6.70×10^2	3.42×10^2	9.88×10^5	5.04×10^5	
e	$17^h45^m48^s.08$	-28°59′22.″59	9.63 × 5.79	19.13	2.52×10^2	1.29×10^2	3.17×10^6	1.62×10^6	HMC14
f	$17^h45^m48^s.05$	-28°59′40.″91	7.75 × 4.69	10.08	2.31×10^3	1.18×10^3	2.00×10^6	1.02×10^6	
g	$17^h45^m47^s.81$	-28°59′52.″50	7.28 × 4.37	8.18	1.22×10^3	6.21×10^2	2.00×10^6	1.02×10^6	
h	$17^h45^m50^s.45$	-29°00′05.″83	2.96 ×2.32	1.42	9.87×10^2	5.04×10^2	1.98×10^6	1.01×10^6	HMC24 or HMC25
i	$17^h45^m51^s.34$	-29°00′15.″20	9.44 × 4.80	13.06	1.71×10^2	8.73×10^1	3.43×10^6	1.75×10^6	HMC27
j	$17^h45^m51^s.08$	-28°59′27.″82	2.73 × 1.56	2.64	1.58×10^3	8.04×10^2	1.30×10^6	9.54×10^5	north of HMC15
H42α				(mJy km s^{-1})					
HCHII	$17^h45^m51^s.02$	-28°59′29.″48	2.16 × 1.58	7.48	—	—	—	—	source j H42α emission

level. Four other lines of CH_3OH, i.e., (J_{K_a,K_c}=$2_{-1,2}$-$1_{-1,1}$ E: 96.73936 GHz), (J_{K_a,K_c}=$2_{0,2}$-$1_{0,1}$A$^+$: 96.74138 GHz), (J_{K_a,K_c}=$2_{0,2}$-$1_{0,1}$E: 96.74455 GHz), and (J_{K_a,K_c}=$2_{1,1}$-$1_{1,0}$E: 96.75551 GHz), are blended with each other and hence are not used in our analysis. The other line, CH_3OH (J_{K_a,K_c}=$6_{-2,5}$-$7_{-1,7}$E: 85.56808 GHz), is detected as an absorption line. It is known to become a Class-II maser line in some conditions (Cragg et al. 2005) and hence is ignored here. The observed frequency bands include several v_t=1 high-excitation transitions of the above-mentioned CH_3OH lines, which would be emitted from the cores with a high gas temperature (e.g. Barnes et al. 2019). However, they are not detected in our observed

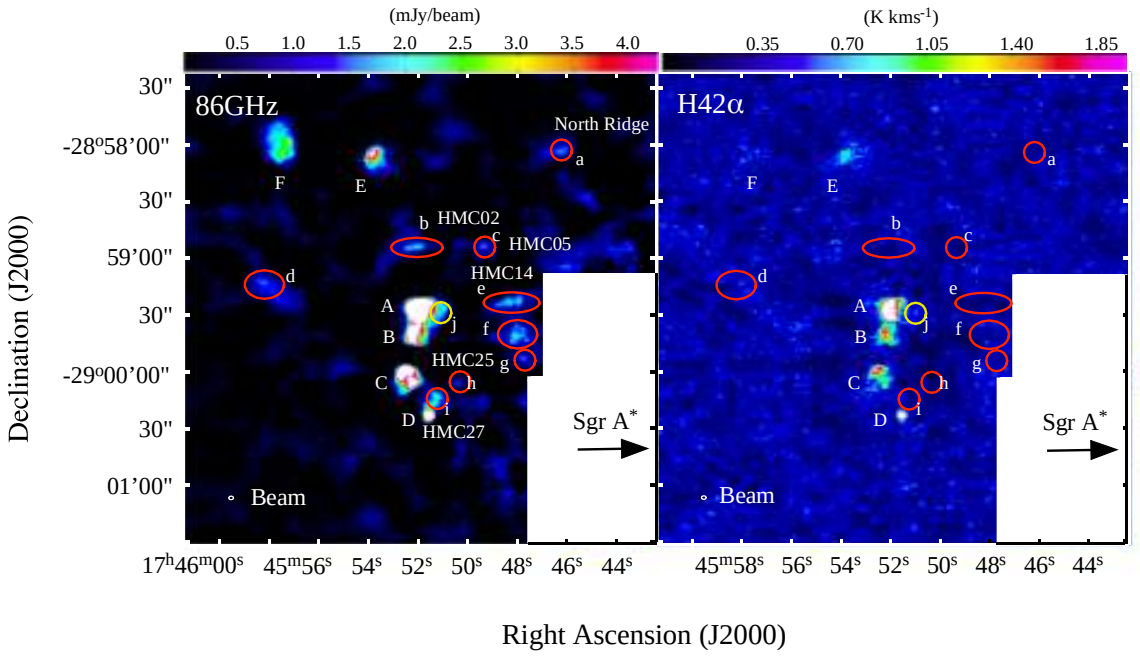

Fig. 2. Observed (Left panel) 86-GHz continuum and (Right panel) H42α integrated maps, together with the intensity color-scale bars at the top of each panel. The prominent 8.4-GHz sources A, B, C, D, E, and F (Mills et al. 2011) are labeled. The known sources a–i in dust-continuum emission and H42α source j are indicated with red and yellow circles, respectively. The angular resolution is 2.″49×1.″85 (PA=−89.°70). The beam size is indicated at the bottom left corner of each panel.

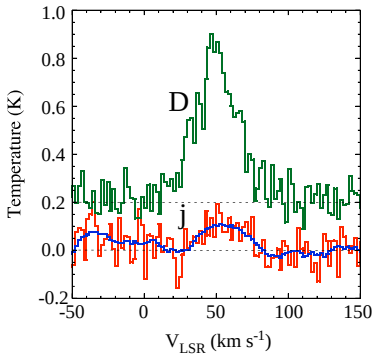

Fig. 3. H42α line profile toward (green) HII D and (red) source j in Figure 2. The 11 ch smoothed intensities are overlaid on the latter in blue.

dust cores and HMCCs.

The other line of our interest is the $HC^{15}N$ emission line. It is optically thin, has a high critical density of $\sim 10^7$ cm^{-3} (e.g. Rolffs et al. 2011), and has been used as a probe for high-density and warm cores. Boonman et al. (2001) reported that the HCN emission line is enhanced in the dense regions that are at the stage evolving from gravitationally bound cores to HMCs. Moreover, Stéphan et al. (2018) modeled the spatio-temporal evolution of the chemistry of HMCs and their simulation showed significant $HC^{15}N$ and CH_3OH line emissions from warm core. Line emissions from HMCs are not decreased during the evolution of the cores. Since the abundance ratio of $^{14}N/^{15}N$ varies greatly between 70 and more than 1000 as in prestellar cores (e.g. Ikeda et al. 2002), the $HC^{15}N$ emission often becomes weak. The line profiles of HMCCs at the SO emission line are similar to the $HC^{15}N$ emission line(Schilke et al. 2001). Consequently, $HC^{15}N$ is a good tracer of a dense and warm core.

Many theoretical and observational studies have been conducted on HMCs; they are generally categorized into two models: a core model with a dust sublimation zone in the vicinity of the central source (Central Source Model: CSM) and another core model in which some external source warms the core (External Source model: ESM) (e.g. Kauffman et al. 1998). In the HMC in the CSM, HMPO or earlier HCHII is placed in the center. The ESM is often preferred with observational results of HMCs with UCHIIs. In the ESM model, HMCs may be formed in situations where some shock compresses the molecular gas, resulting in gravitational collapse of the dense core. Nomura &

Millar (2004) studied the evolution of the molecular abundance in HMCs and the abundance ratio of the radius. SO molecules generally increase in abundance as approach the central source. It is known that the abundance of SO is a decreasing function of the radius. The abundances of SO and CH_3OH are enhanced by ice evaporation and shock, both of which are triggered by molecular outflows (e.g. van der Tak et al. 2003). Then, the intensity of the emission line may vary even when the temperature is the same. Specifically, in the CMZ, the abundance of SO may have increased due to other shocks. Hence, a HMC can be present near the peak, and a weak filamentary structure may be observed in the vicinity. We should distinguish the SO emission of HMCCs from others such as turbulence and shock caused by CCC.

Tsuboi et al. (2015a) found a half shell-like feature with a high temperature ratio of T(SiO)/T($H^{13}CO^+$) in the 50 MC. Given that the abundance of SiO is increased by a C-shock in molecular clouds whereas that of $H^{13}CO^+$ is not affected by the shock (e.g. Amo-Baladrón et al. 2011), the feature would be evidence of shock wave propagation in the cloud. Barnes et al. (2019) reported signs of embedded star formation in Clouds D and E/F of a part of the CMZ and detected the SO ($N_J = 3_4$ - 4_3) emission, notably from Cloud E. Their images were compact to the extent that the target was not sufficiently resolved with the spatial resolution of their observation of Cloud E ($1\farcs27 \times 0\farcs90$ (PA=$0\fdg0$)), whereas the peak in their images of SO ($N_J = 5_6 - 4_5$) was only moderately compact with weak environment emission. Barnes et al. (2019) suggested that the cores in Clouds D and E/F had evolved both physically and chemically and that molecules such as SO had probably originated from regions that harbored embedded star formation (e.g., due to strong shock).

Therefore, comparisons among the SO, CH_3OH and $HC^{15}N$ lines, which will be discussed later, can provide clear indication of whether the HMCCs have denser and warmer conditions than the cores observed with the CS and $H^{13}CO^+$ emissions.

3.3 Identification of HMCCs

3.3.1 HMCCs

Figures 4a and 4b show the velocity channel maps of the SO emission superimposed on the 86-GHz continuum map. Each channel map is integrated over 2.0 km s^{-1} width centered on the velocity indicated in each panel of the figures. We identify many filament-like structures over a velocity range of $V_{\rm LSR}$=−14 to 84 km s^{-1} in the SO emission line. There are many various peaks with small sizes and broad velocity widths in the filaments. Many of the peaks appear to be connected by weak bridge components in both spatial and velocity domains. HMCs are thought to have a tendency to be located at such peaks and to be buried into the surrounding cool static ambient gas. In order to identify HMCCs, it is necessary to distinguish between warm HMCCs and cold envelopes, using their line profiles.

In the typical HMC object Orion KL, the line profile of the SO emission line consists of distinct two components, "hot core" and "plateau" (e.g. Plambeck et al. 1982; Wright et al. 1996), in addition to considerably weaker components, "compact ridge" and "extended ridge", whose contributions are secondary or less and are usually ignored. The "hot core" and "plateau" components are generally considered to correspond to the HMC and cold envelope, respectively (e.g. Wright et al. 1996). van der Tak et al. (2003) showed that the SO ($N_J = 6_6 - 5_5$ and $8_7 - 7_6$) emission profiles from the regions of HMCs had high and low-velocity components and suggested that they correspond to, respectively, the "hot core" and "plateau" mentioned above. Assuming that the SO emission line profiles of HMCs generally have the "hot core" and "plateau", we divide the observed line profiles of the regions of HMCCs into the HMC and cold envelope components including filaments in this section. We note that the SO emission from filaments, which appear at a velocity band from V_{LSR}=30 km s^{-1} to 60 km s^{-1} (Figure 4), is mostly weak and hence that the HMC components are detectable in high-intensity regions only.

3.3.2 Identification by "clumpfind" and Visual Inspection

One of the popular algorithms to identify HMCCs is "clumpfind" (Williams et al. 1994), which we adopt in this section. We first validate how suitable "clumpfind" is for our purpose. The "clumpfind" decomposes structures with a set of elliptical Gaussians. Although the SO emission may not be strictly a combination of Gaussian structures, the structure of the line from the HMCCs will not be anyhow resolved with a sufficiently high resolution in our data, given that our beam is only slightly smaller than the spatial extent of the HMCCs.

Li et al. (2020) recently made a quantitative comparison of the performance of popular algorithms for molecular-gas-clump identification, including GaussClumps (Stutzki & Guesten 1990), clumpfind, Fellwalker (Berry 2015), Reinhold developed by Kim Reinhold, and Dendrograms (Rosolowsky et al. 2008). Designing simulated clumps of various sizes, peak brightness, and crowdedness, Li et al. (2020) concluded that Fellwalker, Dendrograms, and GaussClumps performed better with regard to detection completeness and also found that the average deviations in clump parameters gradually increase with any of the algorithms as the size and Signal-to-Noise Ratio of clumps increase. Li et al. (2020) also showed that "clumpfind" identified the cores with sufficient precision, although the score on some tests with "clumpfind" is not better than the others. They suggested that it was difficult to identify cores in an automated way. Bearing in mind the points raised by Li et al. (2020), we manually identify HMCCs from the searched HMCC1s (only idenfied by "clumpfind"), using "clumpfind",

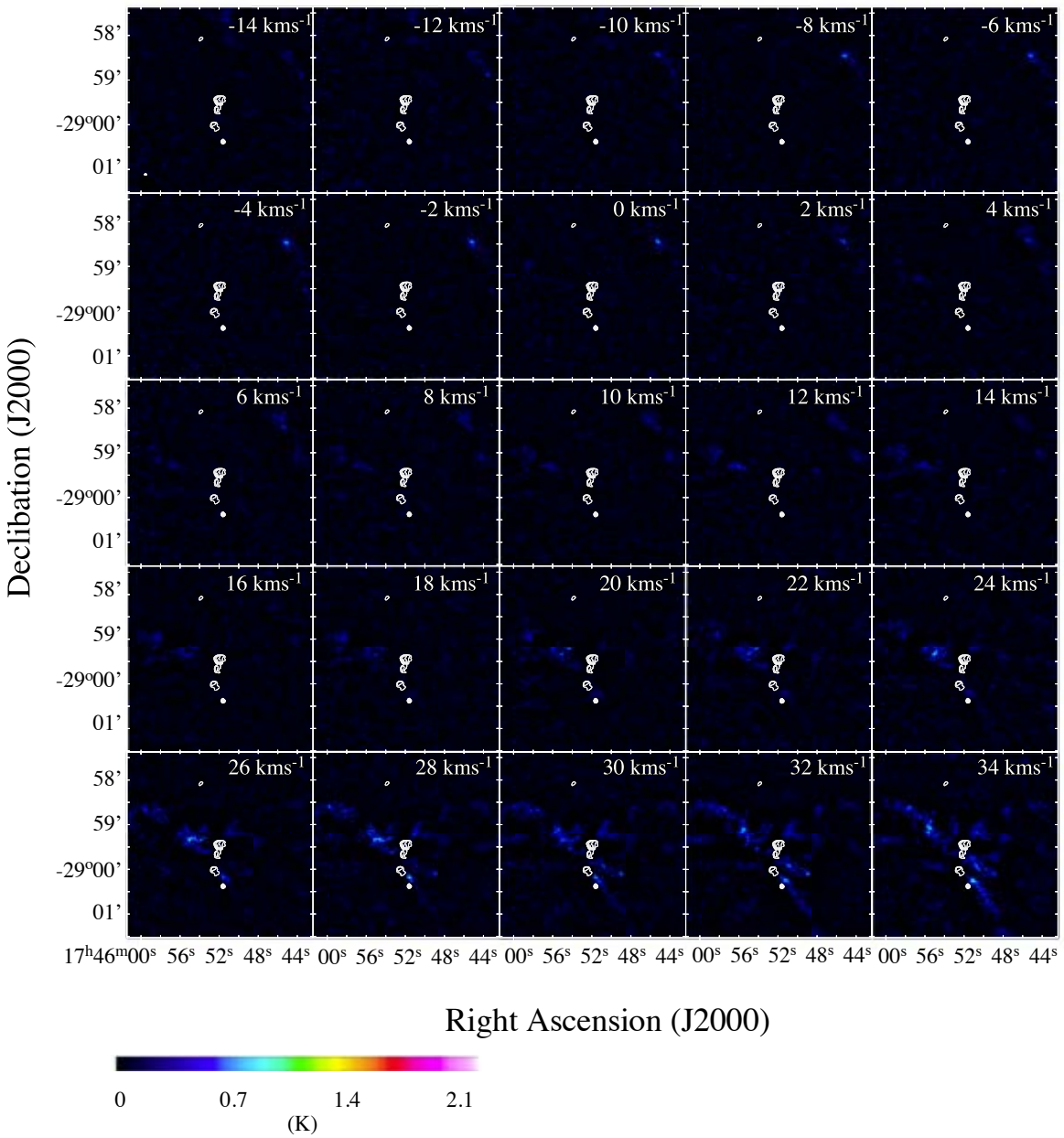

Fig. 4a. SO velocity-divided color-image maps with a uniformly-weighted angular resolution of 2.″49×1.″85 (PA=−89.°70). The center velocity in V_{LSR} (km s^{-1}) is shown at the upper-right corner of each map. The peak specific-intensity is 2.25 K. The typical rms noise level is 35.4 mK. The 86-GHz continuum image is overlaid with linearly-spaced white line contours with the levels from 10% to 90% with intervals of 10 points.

in the following procedures.

1. To find HMCCs, we use the "clumpfind" software to identify clumps on the SO, ^{34}SO, HC^{15}N, and CH_3OH emission maps. We use 20σ and 10σ as the lowest contour (threshold) and contour spacing, respectively, for the first three emission lines, and 40σ and 20σ, respectively, for the CH_3OH emission line. The 1σ level is 35.4 mK in any of the maps. These parameters are selected in such a way that it would be easier to distinguish the static gas from the low and high-velocity components of the HMCs with the criteria of a small ra-

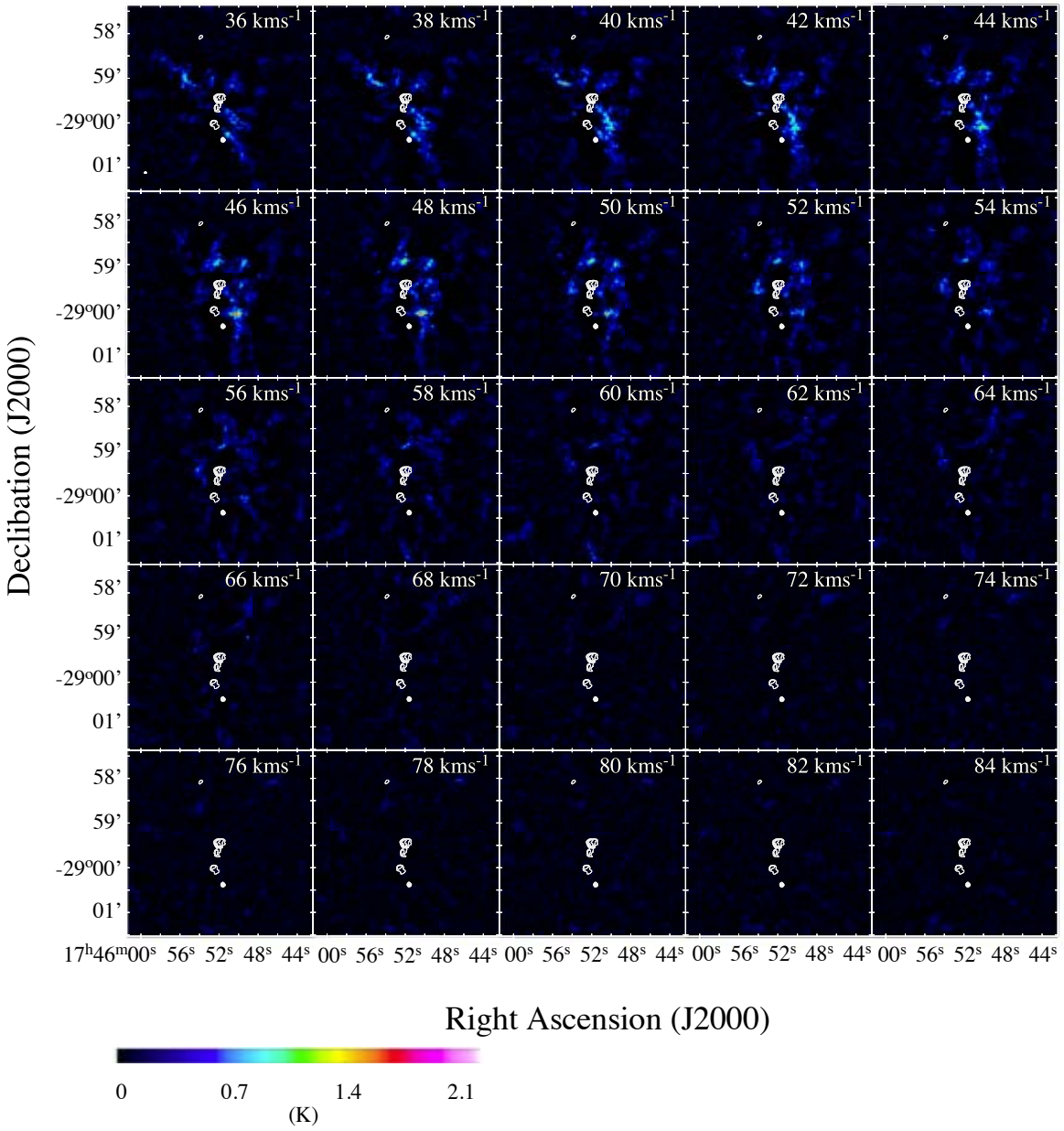

Fig. 4b. continued

dius and weak intensity (van der Tak et al. 2003). Moreover, HMCC1s are identified with criteria of small radius ($r < 10''$) and weak intensity ($T > 700$ mK). The derived parameters of the HMCC1s are summarized in Table 2.

2. If one HMCC1 is located within $5''$of another HMCC1 and the velocity difference between the two HMCC1s is smaller than 10.0 km s^{-1}, we regard the two HMCC1s as the same HMCC1.
3. The identified HMCC1s are classified into the three groups of isolated HMCC1s, HMCC2s, and HMCC3s. The HMCC2 has two velocity components with similar isolated positions, and the HMCC3 has three or more velocity peaks (e.g. Jiménez-Serra et al. 2012). A HMCC3 would be more reliable as a HMCC than an isolated HMCC1 and HMCC2

because the spectra of HMCCs have been reported to have usually several peaks in the molecular emission lines, e.g., SO and CH_3OH ones. Thus, we first identify HMCCs in the regions of the HMCC3s and then examine the HMCC2s and HMCC1s, using "clumpfind". Figure 5 schematically illustrates how HMCC1s are identified using "clumpfind" (Williams et al. 1994) on the SO emission maps with a certain threshold. Scattering HMCC1 is assumed to be due to physical and chemical reaction in the HMC because Jiménez-Serra et al. (2012) showed that there are two chemical groups (Type II and Type III) in the SO and CH_3OH distributions.

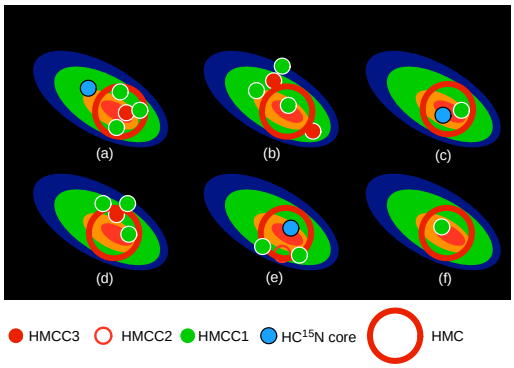

Fig. 5. Identification of HMCCs. HMCC1s are identified using "clumpfind" (Williams et al. 1994) on the SO, ^{34}SO, and $HC^{15}N$, and CH_3OH emission maps with a certain threshold for each line. If one HMCC1 is located within 5.″00 of another HMCC1 and the velocity difference between the two HMCC1s is smaller than 10.0 km s^{-1}, we regard the two HMCC1s as the same HMCC1. A HMCC2 has two velocity components with similar positions, and a HMCC3 has three or more velocity peaks. HMCCs are mainly identified into one of the following six types: (a) Peak in the integrated intensity map having a HMCC3, (b) Peak located between two HMCC3s or more than three HMCC3s, (c) Peak having both HMCC1 and $HC^{15}N$ cores, (d) Peak located near HMCC3, (e) Peak having a $HC^{15}N$ core and located near HMCC2, (f) Peak identified as a HMCC1 with visual inspection.

Tables 2 and 3 list the identified HMCCs. The peak positions of the SO, ^{34}SO, $HC^{15}N$, and CH_3OH emission lines agree with one another for some but not all HMCC1s. The peak positions of the ^{34}SO emission line of the HMCC3s are well correlated to those of the SO emission line. By contrast, those of the $HC^{15}N$ and CH_3OH emission lines of the HMCC1s do not show a good correlation with those of the SO emission line. The positions of the HMCCs cannot be precisely determined within the uncertainty of 5″ because of the differences in the peak locations of the observed emission lines. To identify HMCCs definitively, visual confirmation is necessary.

4. Although mass and size measurements with "clumpfind" are reported to be broadly consistent with those with other methods in general (e.g. Kauffmann et al. 2010a, 2010b), those with "clumpfind" in our work turns out not to be sufficiently so (Pineda et al. 2009). Since our results show several peaks in the HMCCs, the masses of the entire HMCCs are not able to be estimated with the results with "clumpfind". We compile the final list of the HMCCs by selecting visually the ones for which a separation between the peaks of emission lines is smaller than 5″ in HMCC3s or HMCC2s, using the channel maps and/or integrated intensity maps averaged over 10 km s^{-1}. Figure 6 shows a peak velocity map of the SO emission. At 15σ or higher, the distribution of the SO molecular emission is limited, and a considerable amount of filament structure can be eliminated. These are considered to indicate the HMC and its envelope component. The identified HMCCs are mainly classified according to their locations and velocities out of the eight regions named "Northern Ridge", "North", "Northeast", "Northwest", "East", "West", "Southeast", and "Southwest". The HMCC in "Northern Ridge" are regarded as typical HMCCs as described later.
5. Using the HMC in "Northern Ridge" as a template, we identify 28 HMCCs including 19 HMCC3s in the area excluding "Northern Ridge". They are referred to as HMCs 01–28 hereafter. Table 3 tabulates their positions, sizes, peak intensities, peak velocities, line widths, and integrated intensities. Note that the sizes are estimated with 2-dimensional Gaussian fitting with CASA. The estimation of these physical quantities will be further investigated in the next section. The fact that the typical size of the HMCCs, r∼0.1 pc or smaller, is as small as the beam-size, 3″, at the source distance of our observations implies that the calculated quantities have large uncertainties.

Figure 7 shows the positions of the HMCCs identified with the SO, ^{34}SO, and CH_3OH emission lines superposed with the 86-GHz continuum contour map, for which the angular resolution is $2.''49 \times 1.''85$ (PA=$-89.^\circ70$), where uniformly weighted visibility data are selected. The figure also includes the positions of the dense molecular-cloud cores identified with the $HC^{15}N$ emission lines (our work and that by Uehara et al. (2019)) and those of the Class-I CH_3OH masers at 44GHz, Class-I CH_3OH masers at 36GHz (Yusef-Zadeh et al. 2013; McEwen et al. 2016), OH masers (Sjouwerman & Pihlström 2008; Pihlström et al. 2011; Cotton & Yusef-Zadeh 2016), and H_2O masers (Lu et al. 2019a). We find that the spacial distribution of the positions of the HMCC1s identified with the SO and ^{34}SO emission lines are similar to the results identified by "clumpfind" with the $HC^{15}N$ and CH_3OH line emissions.

We examine the identified HMCCs with the SO emission with regard to the following four points.

- Whether the position of the identified HMC with the SO emission agrees with that of a HMCC3 within 5″ or not?
- Whether the HMCC is located between two HMCC3s or not?

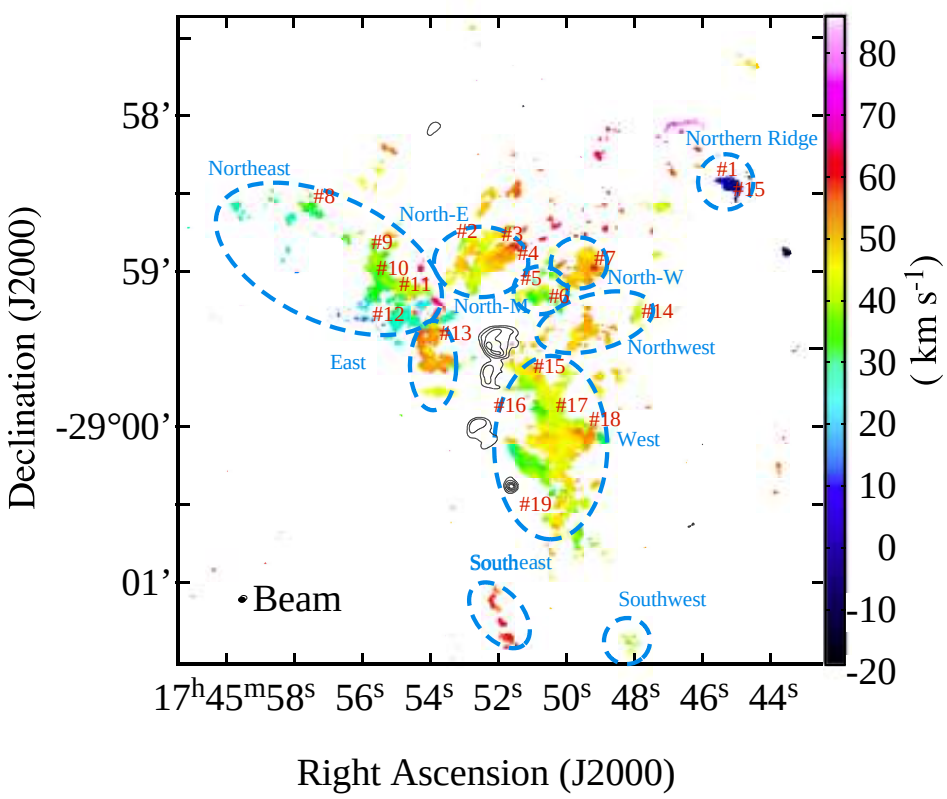

Fig. 6. Peak velocity shift of the SO emission from the average of the region. Only the regions with a velocity larger than 15σ (1σ is 35.4 mK) are plotted. The 86-GHz continuum map, which has a uniformly weighted angular resolution of 2.″49×1.″85 (PA=−89.°70), is overlaid with linearly-spaced contours with levels from 10 to 90% of the peak 41.1 mJy beam^{-1}, or 1.23 K, with intervals of 10 points. Beam size is indicated at the bottom left corner of each panel. The identified regions for clusters of the HMCCs and some selected HMCCs are indicated.

- Whether the HMCC is apparently associated with an HC^{15}N core or not?
- Whether the HMCC is associated with CH_3OH HMCC1 and maser spots or not?

The positions of the HMCC1s identified with the HC^{15}N, CH_3OH, and SO emission lines are found to be well correlated. By contrast, the positions of the CS cold cores (Uehara et al. 2019) agree with three HMCC1s, that is, only 0.3% of the cold cores in the region (3/1061) (Uehara et al. 2021). The results of the positional agreement are included in Table 3.

Figure 8 shows the integrated intensity map of the SO emission line superposed on the 86-GHz continuum map and also plots the positions of the HMMC2s and HMMC3s identified with the SO, ^{34}SO, HC^{15}N, and CH_3OH emission lines using "clumpfind" and those of the Class-I CH_3OH masers (Yusef-Zadeh et al. 2013; McEwen et al. 2016) and OH masers (Sjouwerman & Pihlström 2008; Pihlström et al. 2011; Cotton & Yusef-Zadeh 2016).

Class-I CH_3OH masers in star formation region are known to have a tendency to be associated with shock in protostellar outflow. On the other hand, the ubiquity of the Class-I CH_3OH masers in the CMZ suggests that Class-I CH_3OH masers in this region may be in a different origin, perhaps large-scale shocks from turbulence. Hence, it is necessary to carefully scrutinize the HMCCs that are apparently associated with Class-I CH_3OH masers before making conclusive identification.

OH masers are useful for distinguishing the two possibilities about its origin of outflows and large-scale shocks. Most of the OH masers in the 50 MC are a transition of 1720 MHz whereas the majority of the rest is a transition of 1612 MHz. The OH masers associated with massive star formation regions, known as interstellar OH masers, are strong predominantly in the mainline transitions, i.e., 1665 and 1667 MHz. By contrast, supernova remnants are only associated with 1720 MHz OH masers, which trace the interaction between supernova remnants and surrounding dense molecular cloud (e.g. Frail et al. 1996). Finally, OH masers associated with evolved stars often show double-horned spectral profiles at 1612 MHz. We con-

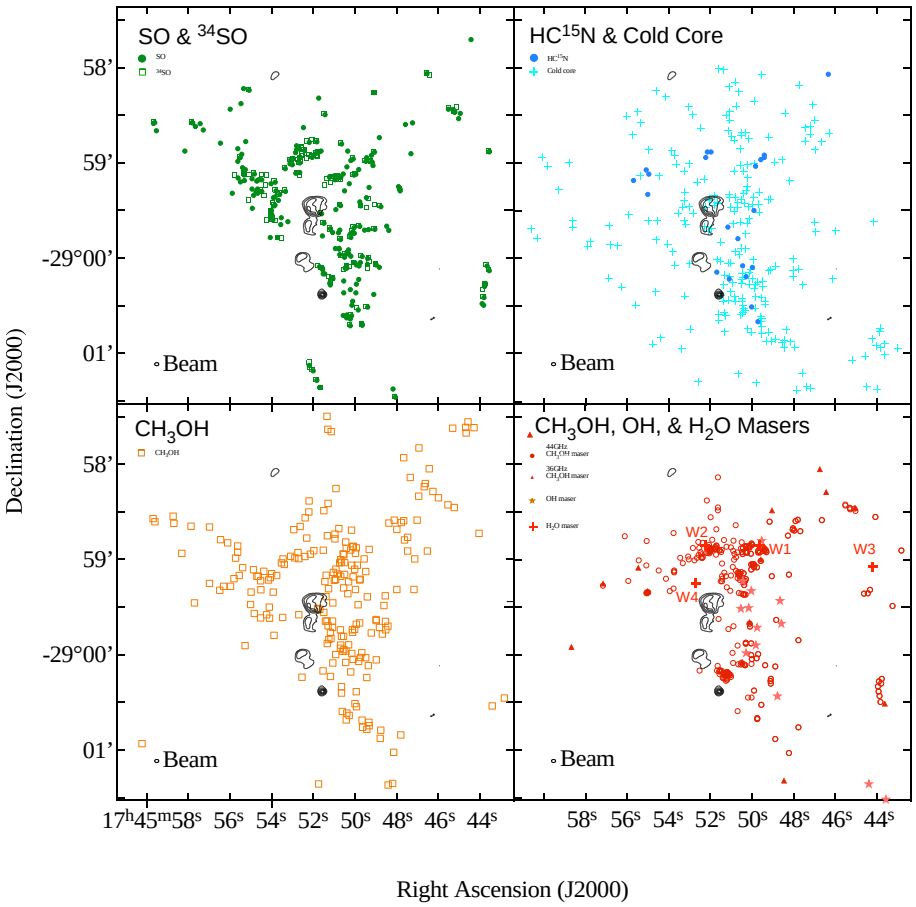

Fig. 7. Positions of the the identified HMCC1s, molecular-cloud cores, and some masers superposed with the 86GHz continuum map at a uniformly weighted angular resolution of $2\farcs49 \times 1\farcs85$ (PA=$-89\fdg70$). The first two groups are identified with the clumpfind algorithm in this work and the last one is taken from literature (see below). The beam size is indicated as an oval on the bottom left corner of each panel. The 86-GHz continuum image is given by the contours with the levels from 10% to 90% of the peak intensity (41.1 mJy beam^{-1}, or 1.23 K, in T_B) with intervals of 10 points. Upper left: Green filled and open circles indicate the positions of the HMCC1s identified with the SO and ^{34}SO emissions, respectively. Upper right: Blue filled circles indicate the positions of dense cores with the HC^{15}N emission (this work), whereas blue crosses indicate cold molecular cores identified by (Uehara et al. 2019). Bottom left: Orange open squares indicate the positions of the HMCC1s identified with the CH_3OH emission. Bottom right: Red open circles, open triangles and red asterisks indicate the positions of 44 GHz Class-I CH_3OH masers, 36 GHz Class-I CH_3OH masers (Yusef-Zadeh et al. 2013; McEwen et al. 2016), OH masers (Sjouwerman & Pihlström 2008; Pihlström et al. 2011; Cotton & Yusef-Zadeh 2016), and H_2O masers (W1–W4) (Lu et al. 2019a), respectively.

clude that there are no OH masers in the 50 MC associated with massive star formation.

H_2O masers also need attention. Four H_2O masers are detected in the area (Lu et al. 2019a). W2 and W4 are associated with star formation, whereas W1 and W3 have Asymptotic Giant Branch (AGB) star counterparts.

3.4 Individual HMCCs

Figures 9a–9f show the enlarged integrated intensity maps in the SO emission line around the 28 identified HMCCs, which are named HMC01–HMC28. The HMCCs are categorized according to their positions into the eight regions: "Northern Ridge", "North", "Northeast", "Northwest", "East", "West",

Table 2. Number of 50 MC Hot Molecular Core Candidates

HMCC	SO	^{34}SO	HC^{15}N	CH_3OH
clumpfind raw	168	22	64	216
Identified HMCC1	110	21	39	84
HMCC2	39	16	-	-
HMCC3	19	8	-	-
HMCC	28(17)	4	10	24

Note: In the clumpfind identification, we adopt a threshold of 20σ and contour spacing of 10σ with a rms value of 35.4 mK for SO, ^{34}SO, and HC^{15}N. For CH_3OH, we adopt a threshold of 40σ and contour spacing of 20σ. The number inside the parentheses indicates the that of the HMCCs identified only from HMCC3s. The numbers in the ^{34}SO, HC^{15}N, and CH_3OH columns indicate those of the HMCs associated with a HMC of SO.

Table 3. Physical Properties of the Hot Molecular Cores in the 50 MC investigated with the SO emission

Region	HMC#	SO HMCC3#	$HC^{15}N$ Core	CH_3OH HMCC1	CH_3OH masers	H_2O masers	86 GHz Dust	Position Right Ascension J(2000)	Position Declination J(2000)	Size Maj×Min arcsec(″)	SO peak S_ν (K)	SO V_{LSR} (km s^{-1})	SO ΔV_{FWHM} (km s^{-1})	SO $\int S_\nu dv$ (K km s^{-1})	^{34}SO peak S_ν (K)	^{34}SO V_{LSR} (km s^{-1})	^{34}SO ΔV_{FWHM} (km s^{-1})	^{34}SO $\int S_\nu dv$ (K km s^{-1})	Note
Northern Ridge		#1	√	√	√		√	$17^h45^m45\overset{s}{.}20$	-28°58′26.″36	7.″64×4.″17	0.40 ± 0.02	-2.6 ± 0.4	18.0 ± 0.9	7.62 ± 0.48	0.19± 0.03	-3.8 ± 1.1	15.9 ± 3.1	3.27 ± 0.77	(1)
North-E	01	#2			√			$17^h45^m52\overset{s}{.}82$	-28°58′50.″61	12.″17×7.″25	0.27 ± 0.02	47.0 ± 0.5	17.4 ± 1.3	4.98 ± 0.48	0.13± 0.02	47.4 ± 1.0	16.4 ± 2.5	2.24 ± 0.44	(2)
	02	(#3, #4)	√	√	√	√	√	$17^h45^m52\overset{s}{.}67$	-28°58′59.″26	12.″22×6.″07	0.37 ± 0.02	40.9 ± 0.3	14.4 ± 0.8	5.76 ± 0.44	0.15 ± 0.02	41.4± 0.9	12.4 ± 2.2	2.02 ± 0.48	(3)
	03			√	√			$17^h45^m52\overset{s}{.}06$	-28°58′54.″07	24.″64×7.″32	0.56 ± 0.03	50.9 ± 0.3	16.2 ± 0.9	9.73 ± 0.68	0.30± 0.02	51.4 ± 0.6	14.2 ± 1.3	4.52 ± 0.55	(3)
North-M	04	(#5, #6)		√	√			$17^h45^m50\overset{s}{.}71$	-28°59′08.″27	8.″53×3.″88	0.35 ± 0.03	36.4 ± 0.6	15.9 ± 1.5	5.98 ± 0.75	0.18 ± 0.03	33.9 ± 1.1	15.5 ± 2.6	2.97 ± 0.66	(3), (4)
North-W	05	(#7)	√	√			√	$17^h45^m49\overset{s}{.}52$	-28°58′59.″26	8.″68×4.″95	0.61 ± 0.03	49.7 ± 0.2	10.0 ± 0.6	6.44 ± 0.48	0.13 ± 0.03	52.5 ± 1.3	15.3 ± 3.5	2.07 ± 0.59	(3)
NorthEast	06	#8						$17^h45^m57\overset{s}{.}65$	-28°58′36.″05	15.″62×6.″74	0.31 ± 0.03	34.1 ± 0.3	7.9 ± 0.8	2.59 ± 0.33	0.16 ± 0.04	33.8 ± 0.7	6.7 ± 1.7	1.14 ± 0.37	(2)
	07	#9		√				$17^h45^m55\overset{s}{.}59$	-28°58′56.″14	10.″70×6.″24	0.55 ± 0.03	38.5 ± 0.3	9.2 ± 0.6	5.36 ± 0.48	0.24 ± 0.02	38.0 ± 0.4	8.6 ± 1.0	2.17 ± 0.59	(3)
	08	#10		√				$17^h45^m55\overset{s}{.}38$	-28°59′03.″41	12.″99×4.″48	0.49 ± 0.03	36.8 ± 0.4	15.1 ± 1.0	7.84 ± 0.66	0.22 ± 0.02	36.3 ± 0.5	11.1 ± 1.1	2.61 ± 0.35	(3)
	09	(#11)	√	√				$17^h45^m54\overset{s}{.}99$	-28°59′05.″49	14.″36×4.″56	0.78 ± 0.04	39.2 ± 0.2	6.8 ± 0.4	5.69 ± 0.50	0.34 ± 0.03	39.5 ± 0.3	5.7 ± 0.7	2.06 ± 0.31	(3,4)
	10		√	√				$17^h45^m54\overset{s}{.}99$	-28°59′20.″38	14.″76×13.″81	0.48 ± 0.02	24.9 ± 0.3	14.2 ± 0.7	7.23 ± 0.50	0.26 ± 0.02	25.5 ± 0.5	13.6 ± 1.2	3.84 ± 0.44	(3,5)
	11			√				$17^h45^m54\overset{s}{.}43$	-28°59′07.″57	7.″71×4.″29	0.47 ± 0.04	40.0 ± 0.3	8.1 ± 0.8	4.04 ± 0.51	0.15 ± 0.02	41.6 ± 0.6	8.7 ± 1.3	1.36 ± 0.28	(2,5)
East	12	(#12, #13?)		√				$17^h45^m54\overset{s}{.}22$	-28°59′21.″08	6.″43×2.″00	0.29 ± 0.02	28.6 ± 0.5	13.0 ± 1.1	3.97 ± 0.46	0.14 ± 0.01	28.6 ± 0.3	6.9 ± 0.7	0.99 ± 0.14	(2,5)
	13	(#13?)						$17^h45^m54\overset{s}{.}12$	-28°59′30.″77	7.″60×4.″91	0.23 ± 0.03	32.5 ± 1.1	16.0 ± 2.6	3.98 ± 0.84	0.08 ± 0.02	35.4 ± 1.5	14.0 ± 3.9	1.25 ± 0.42	(2,5)
NorthWest	14	#14					√	$17^h51^m51\overset{s}{.}56$	-29°59′37.″92	5.″06×3.″00	0.40 ± 0.04	45.4 ± 0.5	9.1± 1.1	3.86 ± 0.61	0.17 ± 0.03	47.4 ± 0.8	10.3 ± 1.9	1.89 ± 0.46	(2)
West	15			√	√			$17^h45^m51\overset{s}{.}56$	-29°59′37.″70	3.″49×3.″25	0.38 ± 0.03	42.6 ± 0.5	12.7 ± 1.2	5.18 ± 0.66	0.17 ± 0.03	42.4± 0.7	12.9± 1.6	2.39 ± 0.40	
	16		√	√	√?			$17^h45^m51\overset{s}{.}24$	-28°59′40.″81	10.″83×6.″35	0.37 ± 0.04	42.2 ± 1.0	15.8 ± 2.2	6.17 ± 1.16	0.17 ± 0.03	39.1 ± 0.7	6.7 ± 1.5	1.23 ± 0.37	
	17	#15		√	√			$17^h45^m50\overset{s}{.}05$	-28°59′43.″68	7.″99×4.″01	0.26 ± 0.02	39.3 ± 0.5	12.0 ± 1.2	3.36 ± 0.46	0.10 ± 0.02	38.5 ± 1.1	11.6 ± 2.8	1.25 ± 0.42	(3)
	18		√	√				$17^h45^m50\overset{s}{.}74$	-28°59′48.″09	8.″98×4.″92	0.56 ± 0.02	41.9 ± 0.2	10.7 ± 0.5	6.33 ± 0.40	0.28 ± 0.02	42.6 ± 0.3	8.5 ± 0.6	2.50± 0.24	(5)
	19	#16		√	√			$17^h45^m50\overset{s}{.}76$	-28°59′53.″97	10.″71×6.″00	0.37 ± 0.03	35.1 ± 0.5	14.0 ± 1.1	5.45 ± 0.57	0.10 ± 0.01	34.0 ± 0.8	14.3 ± 1.8	1.56 ± 0.26	(2)
	20			√	√			$17^h45^m50\overset{s}{.}32$	-28°59′53.″97	10.″28×6.″22	0.60 ± 0.04	40.2 ± 0.3	8.0 ± 0.7	5.10 ± 0.55	0.25 ± 0.02	40.2 ± 0.4	7.5 ± 0.9	1.95 ± 0.29	(4)
	21	#17		√				$17^h45^m50\overset{s}{.}50$	-28°59′58.″13	3.″12×2.″39	0.48 ± 0.02	41.3 ± 0.3	14.0 ± 0.7	7.09 ± 0.48	0.20 ± 0.03	41.8 ± 0.7	10.3 ± 1.7	2.15 ± 0.48	(3)
	22			√	√			$17^h45^m49\overset{s}{.}81$	-28°59′59.″17	11.″16×3.″80	0.32 ± 0.02	42.0 ± 0.7	20.1 ± 1.7	6.96 ± 0.77	0.12 ± 0.02	38.1 ± 0.8	8.4 ± 1.9	1.08 ± 0.31	(3,5)
	23			√	√			$17^h45^m50\overset{s}{.}00$	-29°00′00.″90	8.″17×6.″35	0.42 ± 0.02	46.2 ± 0.5	19.9 ± 1.1	8.89 ± 0.66	0.18 ± 0.04	41.1 ± 1.0	10.2 ± 2.4	1.96 ± 0.62	(3,5)
	24	#18	√	√	√		√	$17^h45^m49\overset{s}{.}81$	-29°00′04.″36	6.″71×5.″45	0.33 ± 0.02	42.0 ± 0.7	20.0 ± 1.6	6.94 ± 0.75	0.18 ± 0.04	48.0 ± 0.6	13.4 ± 1.5	2.53 ± 0.37	(3,4)
	25		√		√		√?	$17^h45^m50\overset{s}{.}40$	-29°00′05.″74	7.″53×4.″18	0.89 ± 0.05	46.5 ± 0.4	12.0 ± 0.8	11.35 ± 1.05	0.40 ± 0.03	47.8 ± 0.3	9.0 ± 0.7	3.86 ± 0.42	(3,5)
	26			√	√			$17^h45^m49\overset{s}{.}45$	-29°00′07.″13	15.″10×7.″87	0.33 ± 0.03	49.8 ± 0.9	19.9 ± 2.4	7.03 ± 1.05	0.17 ± 0.02	51.3 ± 1.0	15.7 ± 2.4	2.75 ± 0.55	(3,4,5)
	27		√	√	√		√	$17^h45^m51\overset{s}{.}16$	-29°00′12.″32	10.″47×5.″69	0.45 ± 0.03	37.4 ± 2.5	22.5 ± 5.8	10.68 ± 2.96	0.23 ± 0.02	34.5 ± 0.8	16.7 ± 1.8	4.19 ± 0.59	(3,4)
	28	#19		√				$17^h45^m50\overset{s}{.}29$	-29°00′37.″25	13.″14×6.″58	0.34 ± 0.01	45.5 ± 0.3	16.4 ± 0.8	5.95 ± 0.37	0.18 ± 0.02	43.9 ± 0.9	14.2 ± 1.6	2.68 ± 0.40	(2)

Note: (Column 3) Indicating the SO HMCC3 number, where its position should satisfy the criterion of falling within 5.″00 of the corresponding HMC position; if not, the number is displayed in a pair of parentheses. (Column 4) Check mark means that the position of the $HC^{15}N$ core agrees with that of a HMC within 5.″00. (Column 5) Check mark means CH_3OH masers found within 5.″00. Peak intensities and Integrated intensities of the SO and ^{34}SO lines are obtained for the 3.″00 beam. The rms noise level is 35.4 mK. The numbers in the "Note" column indicates one of the following: (1) being at Northern Ridge e.g. Takekawa et al. (2017a), (2) being weak, (3) constituting a cluster?, (4) having absorption at the red or blue wing, (5) having two velocity components.

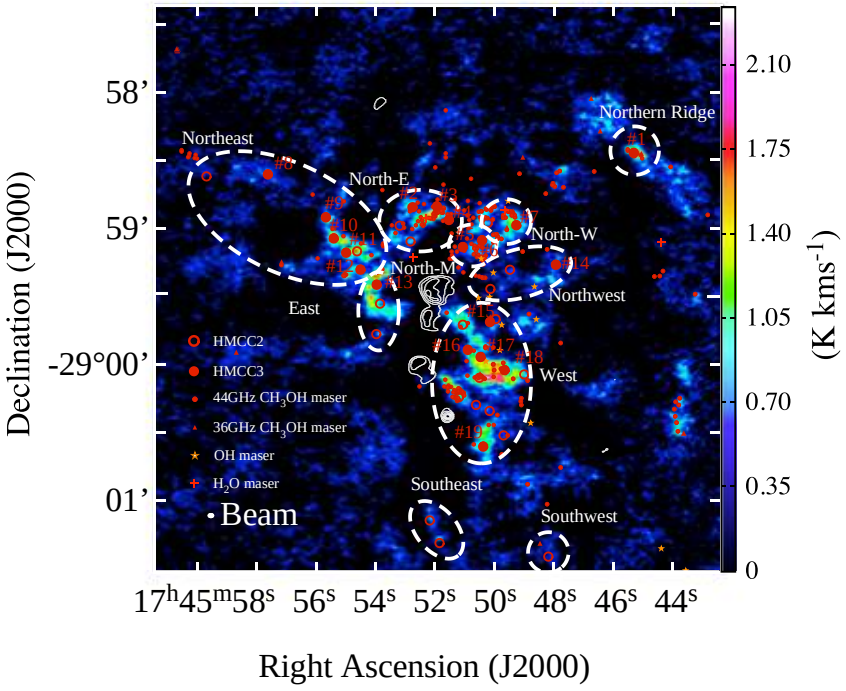

Fig. 8. Velocity-integrated (moment 0, from −14 to 86 km s^{-1}) intensity color-scale map of the SO emission line with a uniformly weighted angular resolution of 2.″49 × 1.″85 (PA=−89.°70). The peak specific intensity is 12.32 K km s^{-1}. The typical rms noise level is 0.18 K km s^{-1}, or 1 mJy beam^{-1} km s^{-1}. White contours show the 86 GHz continuum image with the levels from 10% to 90% with intervals of 10 points. The beam size is indicated at the bottom-left corner. Red small open circles, red filled triangles, and orange asterisks indicate 44-GHz Class-I CH_3OH masers, 36-GHz Class-I CH_3OH masers (Yusef-Zadeh et al. 2013; McEwen et al. 2016), OH masers (Sjouwerman & Pihlström 2008; Pihlström et al. 2011; Cotton & Yusef-Zadeh 2016), and H_2O masers (Lu et al. 2019a), respectively. Red filled and large open circles indicate HMCC3s and HMCC2s, respectively.

"Southeast", and "Southwest". Each has a characteristic distribution; for example, the distributions of $HC^{15}N$ cores and CH_3OH masers are varied. The velocity range is 10 km s^{-1}, and that set so as to include the velocities of the HMC. There are 19 identified HMCC3s, which are numbered HMCC3#1–HMCC3#19. Those are indicated as #1–#19 in Figures 9a–9f.

3.4.1 Northern Ridge

Figure 9a shows the Northern Ridge region (see also Figure 8), where only one peak is identified in the SO and $HC^{15}N$ distributions. The peak of SO emission in the center of the figure is a HMCC3 #1 designated as HMC #1 (Table 3) and several CH_3OH masers exist in its close vicinity. HMC #1 is a typical HMC because the SO emission concentrates within 5″ and is apparently associated with CH_3OH masers. HMC #1 has also the same characteristics as HMC in M0.014-0.054 of Tsuboi et al. (2021). A $HC^{15}N$ core is located 30″ northeast of HMCC3 #1 and is associated with a HMCC1.

This HMCC seems to be a part of "Northern Ridge" or HCN−0.009−0.044, which is located in the northeast side of Sgr A East with a filamentary structure (Takekawa et al. 2017a, 2017b). However, "Northern Ridge" is considered not to be physically related to the 50 MC on the basis of different positions and LSR velocities as apparent in Figure 6. A detailed report on the CCC of Northern Ridge in the Galactic Center Arc is presented by Tsuboi et al. (2021).

3.4.2 North: HMCs01–05

Figure 9b shows five HMCCs in "North." This region encompasses six HMCC3s designated as #2 to #7 and is divided into three sub-regions according to their spatial locations and velocities: "North-E", "North-M", and "North-W".

Region "North-E" is located at the east of North and has three HMCC3s of #2, #3, and #4. HMC01 encompassing HMCC3 #2 is a weak HMC with a velocity of 40 km s^{-1} and with a few CH_3OH masers nearby. HMC02 seems to be a single HMCC identified as HMCC1s #3 and #4 with velocities of 50 km s^{-1} and 60 km s^{-1}, respectively; we conjecture that it is because the $HC^{15}N$ emission has several cores with a few CH_3OH masers and an H_2O maser (W2) (Lu et al. 2019a) in the center of the bright peak between HMCC1s #3 and #4. HMC03 has neither HMCC3 nor $HC^{15}N$ core associated and is located between HMC01 and HMC02 with a few CH_3OH masers nearby. This region "North-E" at 40 km s^{-1} and 50 km s^{-1} has a nested

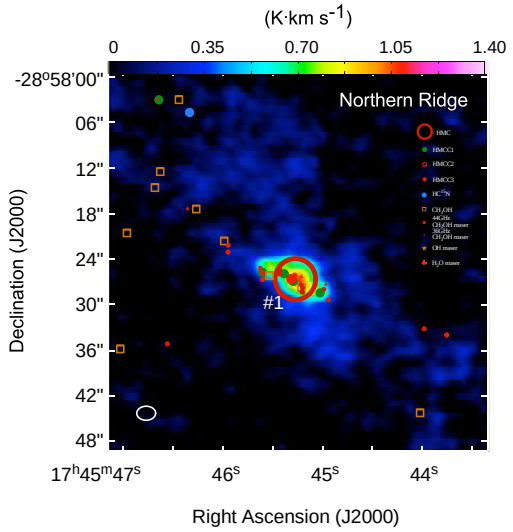

Fig. 9a. Northern Ridge: Color map of the SO velocity-integrated intensity at a velocity of 0 km s^{-1}. The peak intensity is given in Table 2. The typical rms noise level is 18.0 mK km s^{-1}. Max integrated intensities are normalized by 1.19 K km s^{-1} for SO. Beam size is indicated at the left bottom corner. Blue circles, orange squares, green filled circles, red open circles, and red filled circles indicate HC^{15}N cores, CH_3OH, HMCC1, HMCC2, and HMCC3, respectively. Small red filled circles, red filled triangles, orange filled asterisks, and red crosses indicate 44-GHz Class-I CH_3OH masers, 36-GHz Class-I CH_3OH masers, OH masers, and H_2O masers, respectively.

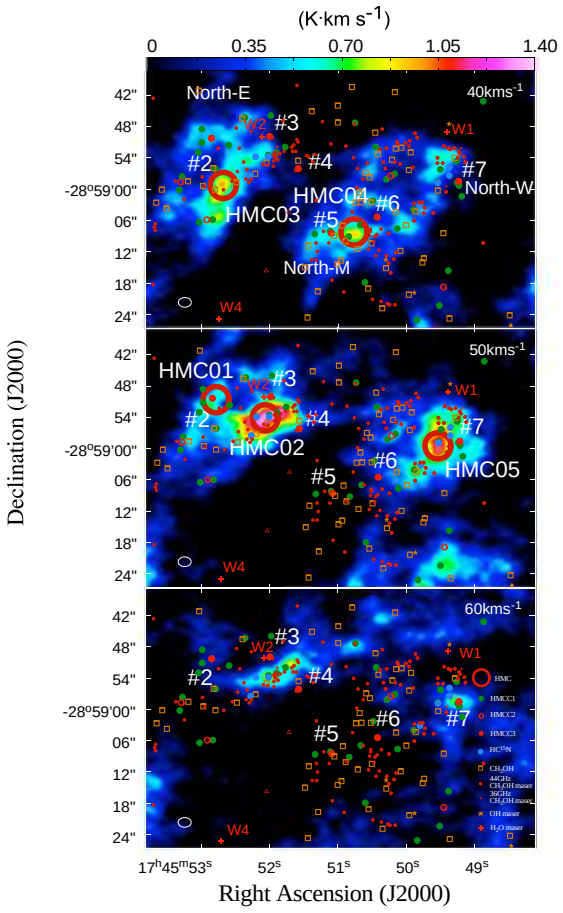

Fig. 9b. Region North: The SO velocity-integrated map at velocities of 40, 50, and 60 km s^{-1}. Color scales and notation are identical with those in Figure 9a.

relation to each other.

Region "North-M" is a group with a velocity of 40 km s^{-1}, which is different from the velocities of 50 km s^{-1} for North-E and -W. HMC04 is located between two HMCC3s #5 and #6 with a separation of 5″ and is apparently associated with several CH_3OH masers.

HMC05 belongs to the group, "North-W", with a velocity of 50 km s^{-1}. HMC05 encompasses three or four HC^{15}N cores with CH_3OH masers. Also adjacent to HMC05 are an OH maser and H_2O maser (W1) associated with an AGB star.

3.4.3 Northeast: HMCs06–11

Figure 9c shows six HMCCs in region "Northeast". These HMCCs are located along a filament running in the northeast to southwest directions and there are five HMCC3s designated as #8 to #12, four HC^{15}N cores, and a few CH_3OH masers in this region. The images at the LSR velocities of 30 and 40 km s^{-1} are similar. HMC06 has a weak peak of HMCC3 #8 with a velocity of 30–40 km s^{-1}. HMC07 has a moderate intensity corresponding to HMCC3 #9 with a velocity of 40 km s^{-1} and no CH_3OH masers nearby. HMC08 corresponds to HMCC3 #10 adjacent to an HC^{15}N core and with no CH_3OH masers nearby. HMC09 has a peak velocity of 40 km s^{-1} with no HMCC1 but HMCC3 #11 located 7″ south, and two HC^{15}N cores exist within 5″. HMC10 has a velocity of 30 km s^{-1} with an HC^{15}N core. HMC10 do not locate on the line of HMCs07, 08, 09, and 11. HMC11 has a weak peak near a HMCC2, which is located 5″southeast.

3.4.4 East: HMCs12, 13

Figure 9d shows two HMCCs in region "East". This region is adjacent to region Northeast but has a different velocity. A weak source, HMC12 corresponding to HMCC3 #12, and HMC13 corresponding to another HMCC3 designated as #13 are located in the north of the crescent structure with a diameter of 15″ at the velocities of 30 and 50 km s^{-1}, respectively. To the south of HMC13, a few HMCC1s are distributed in southern part of the crescent structure, where there is a HMCC2.

H_2O maser W4 is located 15″ east of HMC13. This H_2O maser is not associated with the 50 MC given that the H_2O maser has a peak at 156.0 km s^{-1}.

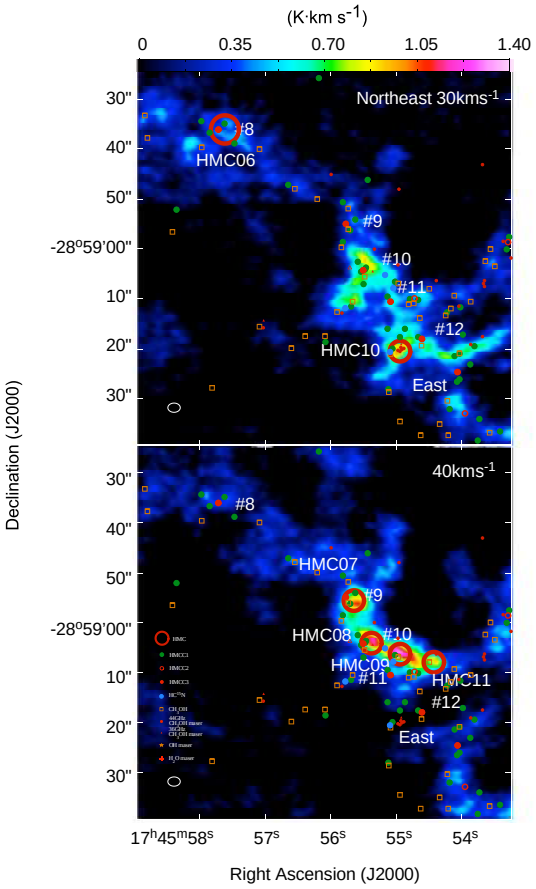

Fig. 9c. NorthEast: The SO velocity-integrated map at velocities of 30 and 40 km s^{-1}. Color scales and notation are identical with those in Figure 9a.

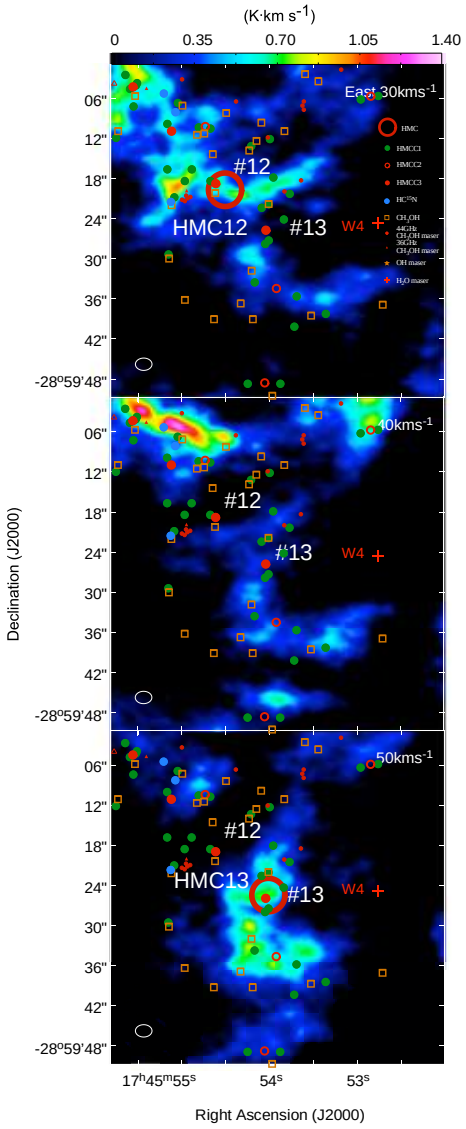

Fig. 9d. East: The SO velocity-integrated map at velocities of 30, 40, and 50 km s^{-1}. Color scales and notation are identical with those in Figure 9a.

3.4.5 Northwest: HMC14

Figure 9e shows a HMC in region "Northwest". This region harbors a weak condensation, HMC14 corresponding to a HMCC3 designated as #14 with a velocity of 40 km s^{-1}. There are no HC^{15}N cores and are a few CH_3OH masers in the region.

3.4.6 West: HMCs15–28

Figure 9f shows 14 HMCCs (#15–#28) in region "West". A half of the HMCCs in this region are located in the upper half (i.e., northern) area with a velocity of 30–40 km s^{-1}, whereas the other half (i.e., southern) is in the lower half area with a velocity of 50 km s^{-1}.

In the northern area, there is a prominent structure of a filament running northeast-southwest that is dominant at a velocity of 40 km s^{-1}; it encompasses diffuse HMC15, HMC16 with an HC^{15}N core, strong HMC18 with an HC^{15}N core, HMC20 with two CH_3OH masers, and HMC22 with a CH_3OH maser. HMC17 is located away from the filament and corresponds to a HMCC3 #15. Diffuse HMC19, corresponding to HMCC3 #16, is also located off the filament. HMC21, corresponding to HMCC3 #17, appears to be linked to HMC19 and belongs to a different filament from the one that encompasses HMCs15–20 and HMC22.

In the southern area, or the central part in the figures, there is weak HMC23 corresponding to HMCC3 #18 with a CH_3OH maser nearby, HMC24 with an HC^{15}N core nearby, and weak HMC26 with a CH_3OH maser nearby, where may bridge HMC22 and HMC23. HMC25 is the strongest HMC in this region with no counterpart HMCC3 but a HMCC2 is located within 5″. HMCs23, 24, 25, and 26 apparently constitute a cluster.

HMC27 is located to the east of the center of the figures

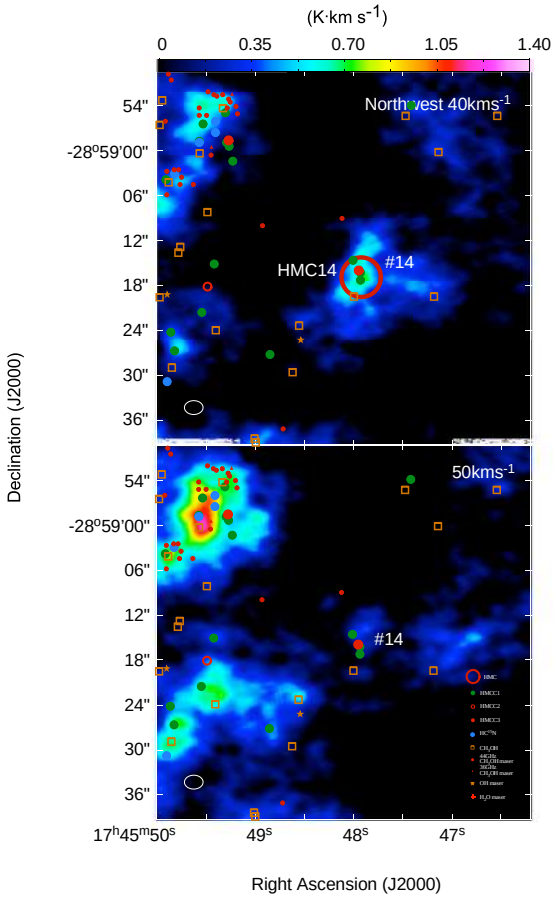

Fig. 9e. NorthWest: The SO velocity-integrated map at velocities of 40 and 50 km s^{-1}. Color scales and notation are identical with those in Figure 9a.

and has unique features; it has no HMCC3 counterparts but a HMCC2 and are apparently associated with two HC^{15}N cores and many CH_3OH masers within 5″. We note that there are HMCC1s with different velocities apparently associated with a HC^{15}N core and a number of CH_3OH masers at 10″ northeast of HMC27 on panels of 30–50 km s^{-1} in Figure 9f. This region has weak SO emission with two velocity components and broad velocity width. It is not clear whether each of these HMCC1s is a HMC or a part of it. HMC27 is located at the northern tip of another filament running northeast to southwest directions, which is connected to HMC28. The southern part of this filament is diffuse, encompassing several isolated HC^{15}N cores and a HMCC1. HMC28 at the bottom of the figures is in a diffuse component and corresponds to HMCC3 #19.

3.4.7 Southeast and Southwest

There are no HMCCs identified in regions "Southeast" and "Southwest". Region Southeast has two weak HMCC2s along a north-to-south filament with a velocity of 60 km s^{-1}. There are four weak SO peaks along a 25″ north-to-south elongated structure, but there are no peaks of HC^{15}N or CH_3OH.

Region Southwest has two weak SO peaks, which are located about 1′ away from region Southeast and has a different velocity of 30 km s^{-1}.

To summarize the results of the eight regions, although some HMCCs are clearly identified in some channel maps, they usually are unclear in the velocity-integrated maps. Some of the HMCCs have good positional correlations between their SO emission and HC^{15}N and CH_3OH emissions, whereas others do not. These results are discussed in detail in §4.1.

3.5 Masses of HMCCs

3.5.1 Masses derived from the 86-GHz continuum emission

The 86-GHz continuum emission of the HMCCs is considered to originate in the dust thermal emission (§3.1.). Then, the mass of the gas can be calculated according to the following equation (Hildebrand 1983):

$$\mathrm{M_d} = \frac{4a\rho D^2 F_\nu}{3B_\nu(T)Q_{125}}(\lambda/125)^\beta, \quad (1)$$

where F_ν is the flux density, B_ν is the the black-body intensity, β is the is the wavelength dependence index, a is the mean grain radius, ρ is the density of dust grain material, D is the distance to the cloud, Q_{125} is the grain emissivity at 125 μm, and λ is the observing wavelength in micron. We adopt the nominal value of 2.0 as the power-law index β, as used in $S_\nu \propto \nu^{2+\beta}$ in the Rayleigh-Jeans domain (Hildebrand 1983). Using the typical values for ρ=3 g cm^{-3}, a=0.1 μm, Q_{125} = 3/4000 (Hildebrand 1983), and T_d =50 K and 100 K, and assuming the typical gas-to-dust mass ratio of 100, the mass of the gas, M_{dust}, is derived to be 1.26±1.55 ×10^3 M$_\odot$ for T_d=50 K and 6.45 ± 8.81 ×10^2 M$_\odot$ for T_d=100 K. Accordingly, the maximum masses of dust cores are 5.45 ×10^3 M$_\odot$ and 2.78 ×10^2 M$_\odot$ at T_d=50 K and T_d=100 K, respectively, whereas the minimum masses of dust cores are 1.71 ×10^2 M$_\odot$ and 8.73 ×10^1 M$_\odot$, respectively. Table 1 summarizes the result.

In the following discussion, we propagate uncertainties of a factor of 2 in the dust masses, which originate from the uncertainties in the dust opacity, gas-to-dust ratio, dust emission flux, and distance to the source, as discussed below. For dust cores with significant internal heating with potentially higher dust temperatures (e.g., higher than T_d=50 K and T_d=100 K, respectively), the derived masses would be systematically lower than the true values. The derived densities of the dust cores depend on the angular sizes and all the quantities that determine the dust masses. The measured angular sizes usually have uncertainties of 20%. We propagate these random errors but exclude the systematic error in the dust temperature and obtain an uncertainty of a factor of 2 for the masses. Similar to the masses, for dust cores with assumed T_d=50 K and T_d=100 K, respectively, the densities would be systematically lower by a factor of 2–3.

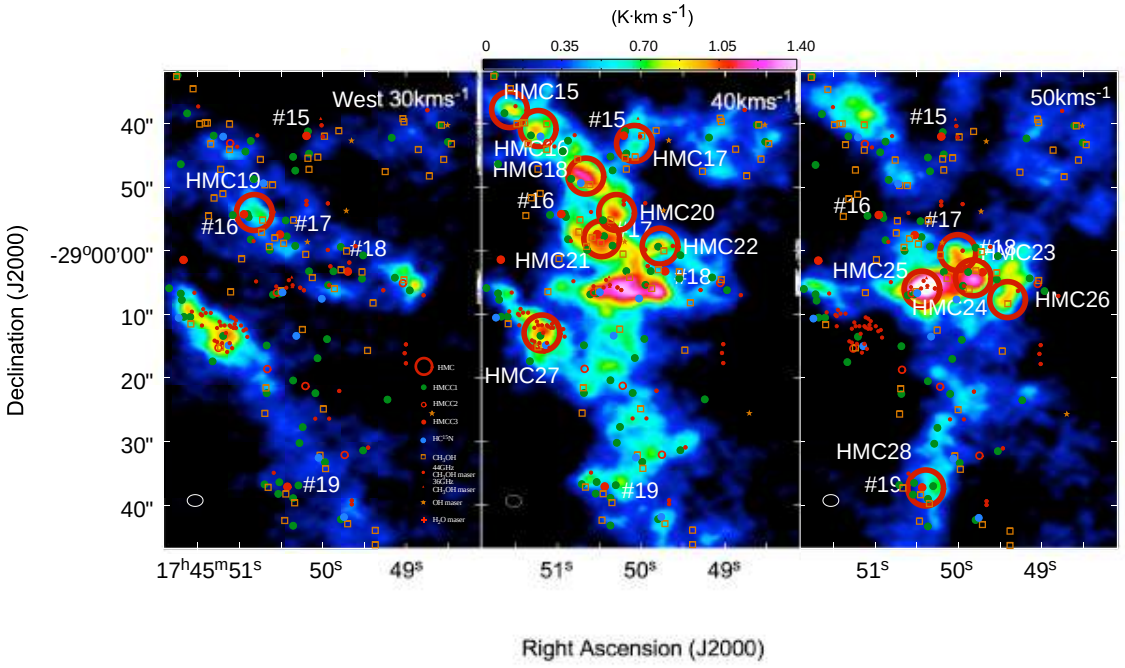

Fig. 9f. West: The SO velocity-integrated map at velocities of 30, 40, and 50 km s^{-1}. Color scales and notation are identical with those in Figure 9a.

3.5.2 Masses derived from the SO emission

Under local thermodynamic equilibrium (LTE) conditions, the column density of a linear molecule can be given by (e.g. Goldsmith & Langer(1999),

$$N(H_2) = \frac{3k}{8\pi^3\nu\mu^2 S}\frac{Q_{\rm rot}}{g_{J+1}} \times \frac{\exp\left(\frac{E_{\rm up}}{kT_{\rm ex}}\right)}{J(T_{\rm ex})}\frac{1}{X(^{32}{\rm SO})} \times \frac{1}{J(T_{\rm ex})-J(T_{\rm bg})}\frac{\tau_{^{32}{\rm SO}}}{1-\exp(-\tau_{^{32}{\rm SO}})}\int S_\nu\, dv. \quad (2)$$

where ν is the frequency of the SO line, $T_{\rm ex}$ is the excitation temperature of SO molecule, $T_{\rm bg}$ is the cosmic background, $\tau_{^{32}SO}$ is the optical depth of ^{32}SO, S is the line strength, SO abundance is X(SO), k is the Boltzmann constant, $Q_{\rm rot}$ is the rotational partition function, the radiation field $J(T)$ is described by the Planck function $B_\nu(T)$, the total degeneracy for an an energy level of a transition is given by the product of rotational g_J degeneracies for rotational molecular transitions, S_ν is the flux densisty, and μ is the permanent dipole moment (1.550D for ^{32}SO). For the N_J=2_2–1_1 transition of ^{32}SO, we have the line strength $S = \frac{J+1}{2J+3} = \frac{2}{5}$ and degeneracy $g_{J+1} = 2J+3 = 5$, where J is the rotational quantum number of the lower state. $E_{\rm up}$ is the energy of the upper state, $E_{\rm up}$=19.31 K. In the calculation, a single excitation temperature was assumed to be 50 K or 100 K (van der Tak et al. 2003). We take the partition function values $Q_{\rm rot}(T)$ = 125 and 250 from the nonlinear plot of The Cologne Database for Molecular Spectroscopy (CDMS) for temperatures of 50 K and 100 K, respectively. We assume a SO abundance of X(SO) = 10^{-9}, given that the SO relative abundance varies in a range of X(SO) ~ (0.5–4)×10^{-9} for various types of HMCCs and has a median value of 1.1–1.3 × 10^{-9} (Li et al. 2015; Zinchenko & Henkel 2018).

Assuming ^{32}SO/^{34}SO=22.5 (Ho & Towns 1983), we have the following intensity ratio,

$$\frac{{\rm I}(^{34}{\rm SO}(2_3-1_2))}{{\rm I}(^{32}{\rm SO}(2_3-1_2))} = \frac{1-\exp(-\tau_{^{32}{\rm SO}}/22.5)}{1-\exp(-\tau_{^{32}{\rm SO}})}, \quad (3)$$

where $\tau_{^{32}SO}$ is the optical depth of the ^{32}SO(2_3-1_2) emission. Our observations show I(^{32}SO(2_2–1_1))/I(^{34}SO(2_3–1_2)) ~2.0. The (2_2–1_1)/(2_3–1_2) intensity ratio of ^{32}SO molecules at both the temperatures is 0.40 from the results of RADEX (van der Tak et al. 2007). As a result, the intensity ratio of I(^{32}SO(2_3-1_2))/I(^{34}SO(2_3-1_2)) is ~5.0. Consequently, $\tau_{\rm SO}$ is calculated to be 4.8, which is moderate optically thick. From the results of RADEX, the optical depth ratio of $\tau_{^{32}{\rm SO}(2_2-1_1)}/\tau_{^{32}{\rm SO}(2_3-1_2)}$ is estimated to be ~1/3, and thus the optical depth of ^{32}SO(2_2-1_1) is ~1.6. Therefore, the correction factor for the LTE mass to correct for the optical depth is derived to be

$$\frac{\tau_{^{32}{\rm SO}}}{1-\exp(-\tau_{^{32}{\rm SO}})} \sim 1.7. \quad (4)$$

The HMCC radius is derived from

$${\rm r(pc)} = \frac{\sqrt{{\rm Maj(pc)}\times{\rm Min(pc)}}}{2} = \sqrt{{\rm r_{Maj(pc)}}\times{\rm r_{Min(pc)}}}. \quad (5)$$

In Table 4, we show the H_2 column density, mean number density, LTE mass derived from the number density assuming a spherical morphology, and virial mass derived from the linewidth ΔV tabulated in Table 3. In consequence, the column densities of the HMCCs are calculated to be N(SO)=6.21

$\pm$ 2.11$\times10^{15}$cm^{-2} for T_{ex}=50 K and 4.95 $\pm$ 1.68$\times10^{15}$cm^{-2} for T_{ex}=100 K. The resultant hydrogen molecule number densities are n(H_2)=1.41 $\pm$ 0.61 $\times10^7$cm^{-3} and 1.12 $\pm$ 0.49 $\times10^7$cm^{-3}, respectively. The LTE masses are estimated to be 1.17 $\pm$ 1.10 $\times10^4$ $M_\odot$ and 9.36 $\pm$ 8.80 $\times10^4$ $M_\odot$, respectively. These values are larger than the mean masses of the $H^{13}CO^+$ and $C^{34}S$ bound cores of 960 $\pm$ 850 $M_\odot$ and 1300 $\pm$ 890 $M_\odot$, respectively (Uehara et al. 2019). The virial masses are estimated to be 9.57 $\pm$ 7.30 $\times10^3M_\odot$, and accordingly the ratios of the LTE mass to the virial mass are 1.412 $\pm$ 0.923 and 1.125$\pm$ 0.736, respectively. We find that 15 HMCCs including the Northern Ridge HMCC have ratios of $\leq$1. The other 14 HMCCs have supercritical masses with a ratio of $\geq$1, where the self-gravity of the HMCCs is likely to be dominant over the internal gas pressure. The bound HMCCs will efficiently form massive protostars if the cores are heated. We note that this result and following discussion would hold regardless of inclusion or exclusion of the Northern Ridge HMC.

The uncertainties of the excitation temperatures of the SO molecules, line fluxes, line widths, and angular sizes, all propagate into that of the derived LTE masses. In our estimate, we have considered a large uncertainty of a factor of 2 for the LTE masses though not considering the systematic error in the excitation temperature. In reality, the abundance X(SO) may be systematically overestimated by a factor of 3 or larger.

The errors of the line widths (20%) and angular sizes (20%) propagate into that of the derived virial masses of the HMCCs. Whereas our estimate has considered a large uncertainty of a factor of 2 or larger, the masses of the HMCCs may be still systematically overestimated by a factor of 3 or larger. It is unclear whether at 0.1 pc the magnetic field is as well as 1.0 pc in the CMZ, where the magnetic field at 1 pc scales in CMZ is suggested to be ~5 mG with large uncertainties (e.g. Pillai et al. 2015). The support against gravitational collapse from the magnetic field would be significant but it is difficult to estimate the strength of the magnetic field in the HMCCs. We note that we ignore the effect of the magnetic field in this paper.

4 DISCUSSION

4.1 Hot Molecular Cores, UCHIIs, and Masers

The lifetimes of HMCs are 10^4–10^5 yr (Herbst & van Dishoeck 2009; Battersby et al. 2017). Those of UCHIIs are ~10^4 yr (Yusef-Zadeh et al. 2010; Tsuboi et al. 2019) and ~10^5 yr to reach a radius of a parsec and to break its parent molecular cloud (Akeson & Carlstrom 1996; Churchwell 2002; Mac Low et al. 2007), respectively. The fact that the HMC exists up to the Hollow HMC (HHMC) stage, which is explained in the next paragraph, in the 50 MC implies that ~10^5 yr has passed since star formation was triggered by CCC.

From a viewpoint of chemical evolution, there is a stage, the Hollow HMC (HHMC), between the HMC and HII region (Stéphan et al. 2018). The "Hollow Hot Core" has the same density structure as the HMC, but it contains a cavity ionized by a HCHII or UCHII at the center. The HHMC has the HCHII or UCHII in the last stage of the HMC (e.g. Furuya et al. 2011; Rolffs et al. 2011; Jiménez-Serra et al. 2012; de la Fuente et al. 2018). As such, the evolutionary stage of the HMC is divided into three stages, "Dense Core", "Hot Core", and "Hollow Hot Core." In the "Dense Core" stage, a warm dense dust core or $HC^{15}N$ core exist at the center. In the "Hot Core" stage, the core becomes warm and dense with a HMPO, which is associated with outflow and disk. In the "Hollow Hot Core" stage, the core consists of either a HCHII or UCHII, probably associated with outflow and disk (e.g. De Pree et al. 2000; Tanaka et al. 2016).

The correlation among the HMCCs, dust cores, $HC^{15}N$ cores, and CH_3OH masers with our data presented in Table 1 and Table 3 provides a statistical basis for estimating the relative timescales of the three stages. The ratios of the HMCCs associated with dust cores, $HC^{15}N$ cores, and CH_3OH masers in our data of 28 HMCCs are 18% (6/28), 32% (9/28), and 54% (15/28), respectively. The ratio of the HMCCs associated with both $HC^{15}N$ and CH_3OH masers is only 18% (5/28), and that with both the H_2O and CH_3OH masers is only 4% (1/28). In the early evolutionary stage, the HMC is assume to be still associated with a dust core or $HC^{15}N$ core, but the dust core soon dissipates. In the intermediate evolutionary stage, the outflow from a protostar in the evolving HMC excites CH_3OH Class-I masers before a HCHII is formed, but CH_3OH Class-II masers are not yet pumped.

Among the samples included in our data, H_2O and Class-I CH_3OH masers were detected in the region of HMC02 whereas no H_2CO masers were detected (Lu et al. 2019b). And SiO (v=2; J=2−1) has not been detected in our observational bands, either. Some indications that H_2O masers are produced in disks have been also reported (e.g. Garay & Lizano 1999; Beuther et al. 2002). Detection of H_2O masers suggests that the region is in an early stage of massive star formation, although we cannot constrain exactly which stage of the HMC the region is in.

Beuther et al. (2002) presented a comparison of Class-II CH_3OH (6.7 GHz) and H_2O (22.2 GHz) masers in a sample of 29 massive star-forming regions. Whereas all masers are associated with massive mm cores, only 3 out of 18 CH_3OH masers and 6 out of 22 H_2O masers are associated with cm emission, the fact of which likely indicates the presence of a recently ignited massive star (Beuther et al. 2002). The Class-II CH_3OH masers are associated with deeply embedded HMPOs or HCHIIs and are excited by warm dust (Pestalozzi et al. 2002; Walsh et al. 2003; Minier et al. 2005). The Class-II CH_3OH and H_2O masers require a similar environment to be excited, but with the different excitation processes (radiative pumping for

Table 4. Masses of the SO Hot Molecular Cores in the 50 MC

Region	HMCC#	50K			100K			LTE Mass (50K) ($M_\odot$)	LTE Mass (100K) ($M_\odot$)	virial Mass ($M_\odot$)	LTE Mass(50K) / Virial Mass	LTE Mass(100K) / Virial Mass	Note
		$N(H_2)$ (cm^{-2})	N(SO) (m^{-2})	$n(H_2)$ (cm^{-3})	$N(H_2)$ (cm^{-2})	N(SO) (cm^{-2})	$n(H_2)$ (cm^{-3})						
Northern Ridge		7.61E+24	7.61E+15	2.10E+07	6.07E+24	6.07E+15	1.67E+07	6.97E+03	5.55.E+03	1.08.E+04	0.646	0.515	C
North-E	1	4.97E+24	4.97E+15	8.23E+06	3.96E+24	3.96E+15	6.56E+06	1.26E+04	1.00.E+04	1.61.E+04	0.783	0.624	C
	2	5.76E+24	5.76E+15	1.04E+07	4.59E+24	4.59E+15	8.29E+06	1.23E+04	9.78.E+03	1.11.E+04	1.107	0.882	S
	3	9.72E+24	9.72E+15	1.13E+07	7.75E+24	7.75E+15	8.98E+06	5.03E+04	4.01.E+04	2.82.E+04	1.784	1.423	S
North-M	4	5.98E+24	5.98E+15	1.62E+07	4.77E+24	4.77E+15	1.29E+07	5.68E+03	4.53.E+03	9.41.E+03	0.603	0.481	C
North-W	5	6.44E+24	6.44E+15	1.53E+07	5.13E+24	5.13E+15	1.22E+07	7.95E+03	6.33.E+03	3.76.E+03	2.113	1.684	S
Northeast	6	2.59E+24	2.59E+15	3.92E+06	2.06E+24	2.06E+15	3.12E+06	7.82E+03	6.23.E+03	2.93.E+03	2.664	2.124	S
	7	5.36E+24	5.36E+15	1.02E+07	4.27E+24	4.27E+15	8.12E+06	1.03E+04	8.19.E+03	4.83.E+03	2.127	1.695	S
	8	7.83E+24	7.83E+15	1.60E+07	6.24E+24	6.24E+15	1.27E+07	1.31E+04	1.04.E+04	1.29.E+04	1.016	0.810	S
	9	5.69E+24	5.69E+15	1.09E+07	4.53E+24	4.53E+15	8.71E+06	1.07E+04	8.52.E+03	2.91.E+03	3.666	2.922	S
	10	7.23E+24	7.23E+15	7.87E+06	5.76E+24	5.76E+15	6.28E+06	4.23E+04	3.37.E+04	1.29.E+04	3.278	2.613	S
	11	4.03E+24	4.03E+15	1.09E+07	3.22E+24	3.22E+15	8.70E+06	3.83E+03	3.06.E+03	2.19.E+03	1.752	1.397	S
East	12	3.96E+24	3.96E+15	1.72E+07	3.16E+24	3.16E+15	1.37E+07	1.46E+03	1.17.E+03	4.74.E+03	0.308	0.246	C
	13	3.98E+24	3.98E+15	1.01E+07	3.17E+24	3.17E+15	8.08E+06	4.27E+03	3.40.E+03	5.66.E+03	0.754	0.601	C
Northwest	14	3.85E+24	3.85E+15	1.54E+07	3.07E+24	3.07E+15	1.23E+07	1.68E+03	1.34.E+03	3.04.E+03	0.553	0.441	C
West	15	5.17E+24	5.17E+15	1.46E+07	4.12E+24	4.12E+15	1.16E+07	4.53E+03	3.61.E+03	5.92.E+03	0.766	0.611	C
	16	6.16E+24	6.16E+15	2.85E+07	4.91E+24	4.91E+15	2.27E+07	2.00E+03	1.60.E+03	3.80.E+03	0.527	0.420	C
	17	3.36E+24	3.36E+15	6.30E+06	2.68E+24	2.68E+15	5.02E+06	6.63E+03	5.28.E+03	6.83.E+03	0.970	0.773	C
	18	6.33E+24	6.33E+15	1.74E+07	5.04E+24	5.04E+15	1.39E+07	5.82E+03	4.64.E+03	4.01.E+03	1.453	1.159	S
	19	5.45E+24	5.45E+15	1.27E+07	4.34E+24	4.34E+15	1.02E+07	6.91E+03	5.51.E+03	7.68.E+03	0.899	0.717	C
	20	5.10E+24	5.10E+15	9.89E+06	4.06E+24	4.06E+15	7.89E+06	9.40E+03	7.50.E+03	3.00.E+03	3.137	2.501	S
	21	7.08E+24	7.08E+15	1.38E+07	5.64E+24	5.64E+15	1.10E+07	1.30E+04	1.04.E+04	8.82.E+03	1.474	1.175	S
	22	6.95E+24	6.95E+15	1.66E+07	5.54E+24	5.54E+15	1.32E+07	8.47E+03	6.75.E+03	1.97.E+04	0.430	0.343	C
	23	8.88E+24	8.88E+15	1.92E+07	7.08E+24	7.08E+15	1.53E+07	1.32E+04	1.05.E+04	1.41.E+04	0.936	0.746	C
	24	6.93E+24	6.93E+15	1.78E+07	5.53E+24	5.53E+15	1.42E+07	7.28E+03	5.80.E+03	1.17.E+04	0.621	0.495	C
	25	1.13E+25	1.13E+16	3.14E+07	9.04E+24	9.04E+15	2.50E+07	1.02E+04	8.17.E+03	4.69.E+03	2.183	1.741	S
	26	7.02E+24	7.02E+15	1.00E+07	5.60E+24	5.60E+15	7.99E+06	2.40E+04	1.91.E+04	2.61.E+04	0.918	0.732	C
	27	1.07E+25	1.07E+16	2.15E+07	8.51E+24	8.51E+15	1.71E+07	1.83E+04	1.46.E+04	2.31.E+04	0.789	0.629	C
	28	5.94E+24	5.94E+15	9.94E+06	4.74E+24	4.74E+15	7.92E+06	1.48E+04	1.18.E+04	7.74.E+03	1.908	1.521	S
Average		6.21E+24	6.21E+15	1.41.E+07	4.95E+24	4.95E+15	1.12E+07	1.17.E+04	9.36.E+03	9.57.E+03	1.412	1.125	S=14
SD		2.10E+24	2.10E+15	6.09.E+06	1.68E+24	1.68E+15	4.86E+06	1.10.E+04	8.80.E+03	7.30.E+03	0.923	0.736	C=15

Column “Note”: S: supercritical mass, i.e., the LTE mass is larger than the virial mass. In this case, the self-gravity of the HMC can overwhelm the gas pressure. Cloud contraction under these circumstances efficiently forms high-mass protostars nearly isothermally even if the core is still being heated. C: LTE mass is comparable with or smaller than the virial mass. In this case, the HMC is either critical or subcritical.

CH_3OH and collisional pumping for H_2O) (e.g. Garay & Lizano 1999; Beuther et al. 2002). Beuther et al. (2002) suggested that the kinematic structures in the different maser species show no recognizable patterns, and failed to draw a firm conclusion as to whether the features are produced in disks, outflows or expanding shock waves. Therefore in the absence of Class-II CH_3OH masers and H_2O masers except in one example, the HMCCs in the 50 MC are likely to be in the early stage of the HMC evolution before the formation of HCHIIs,. As mentioned the above, our proposed evolutionary sequence of the HMCs in the 50 MC is summarized in Figure 10.

If the HMC evolves to a HHMC with HCHIIs and UCHIIs, the observed HHMCs in the 50 MC provide a statistical basis for estimating the relative timescales of these two evolutionary stages. Wilner et al. (2001) argued that the number ratio of the HMCs to UCHIIs is about 50% and suggested that this number ratio tracks the relative lifetimes of the two kinds of objects in W49A, $\tau_{\rm HotCore} \sim 0.5 \times \tau_{\rm UCHII}$. Moreover, Furuya et al. (2005) found that the HMC stage should last less than one-third of the UCHII stage in G19.61−0.23, $\tau_{\rm HotCore} \sim 1/3 \times \tau_{\rm UCHII}$. On the contrary, Miyawaki et al. (2002) presented the result with the SO emission lines from more HMCs adjacent to the UCHIIs in W49A than those studied by Wilner et al. (2001) and concluded $\tau_{\rm HotCore} > \tau_{\rm UCHII}$. The differences between these objects indicates the differences of the evolutionary stage of HMCs that are formed at approximately the same time.

This work, as well as that by Lu et al. (2019a), shows that there are no UCHIIs or HCHIIs in the HMCCs although some HMCCs are located adjacent to UCHIIs. Many CH_3OH Class-II masers are known to be associated with HCHIIs but are no longer associated with UCHII regions (Phillips et al. 1998; Walsh et al. 1998). We conclude that most of the HMCCs in the 50 MC are in the stages between the "Dense Core" and "Hot Core".

4.2 Relation between the Mass and Size

We have concluded that the HMCCs in the 50 MC are in the early evolutionary stage (previous section). We have derived he masses from dust emission, LTE masses, and virial masses with certain uncertainties in §3.5.1 and §3.5.2. In this section, we discuss the relation between the masses and other parameters, in particular the size, of the HMCCs in this stage.

Figure 11 shows the mass-radius relations for the identified HMCCs and dust cores in this work. The masses of the HMCCs and dust cores are found to be proportional to their radii with very small scatters; the former is $M_{\rm LTE}/(M_\odot)$=5.44 $\times 10^5$ $(r/(pc))^{2.17}$ and 4.31 $\times 10^5$ $(r/(pc))^{2.17}$ for $T_{\rm ex}$ = 50 K and 100 K, respectively, and the latter is $M_{\rm dust}/(M_\odot)$=4.28 $\times 10^4$ $(r/(pc))^{2.60}$ and 2.18 $\times 10^4$ $(r/(pc))^{2.60}$ for $T_{\rm d}$=50 K and 100 K, respectively. For the same radius, the mass of the dust core is an order of magnitude smaller than that of the HMCC. The power-law index of the mass-radius relation for the dust cores is slightly larger than that for the HMCCs. Comparison of the mass of the dust core associated with a HMCC to the mass of the HMCC yields a suggestion that X(SO) might be as small as $\sim 10^{-10}$, which is an order of magnitude smaller than our adopted value of 10^{-9} (in §3.5.2). These relations are considerably different from that of molecular clumps, $M(M_\odot) \leq 870\ (r/(pc))^{1.33}$ over a wide range of radius of $0.05 \leq r \leq 3$ pc by Kauffmann et al. (2010b), which is similar to the famous Larson's relation (Larson 1981).

Figure 12 shows the relation between the mean number density and radius for the HMCCs and dust cores; the former is $n(H_2) = 2.65 \times 10^6\ (r/(pc))^{-0.83}$ and $n(H_2) = 2.11 \times 10^6\ (r/(pc))^{-0.83}$ for $T_{\rm ex}$ = 50 K and 100 K, respectively, and the latter is $n(H_2) = 1.11 \times 10^6\ (r/(pc))^{-0.41}$ and $n(H_2) = 5.67 \times 10^5\ (r/(pc))^{-0.41}$ for $T_{\rm d}$=50 K and 100 K, respectively. The number density is found to be a decreasing function of the radius. The slopes of the mean density derived from the dust emission are less steep than those of the HMCCs. If the molecular gas is compressed in one dimension, the number density is expected to obey the proportional relation $n(H_2) \propto r^{-1}$. Hence, the derived slopes for the HMCCs suggest that some mechanism is likely to be in operation to compress molecular gas in one dimension to make the dense HMCCs.

Since the dynamic range of the column density, N(SO), which can be traced with the molecular emission line SO, is narrow, $M_{\rm LTE} \propto r^2 \times N(SO) \propto r^2$ (Figure 11) and $n(H_2) \sim M_{\rm LTE}/r^3 \propto r^{-1}$ (Figure 12). Then, one might suspect that the slopes for the HMCCs in Figures 11 and 12 might be an artifact. However, the four dust cores with the HMCCs show the slope $\sim r^{2.5}$, which is similar to those of the HMCCs. Admittedly, the result is not yet conclusive, given that the number of our sample of HMCCs is limited and only four HMCCs are associated with the dust cores.

The free-fall time, $t_{\rm ff}$, of the HMCC is

$$t_{\rm ff} = \sqrt{\frac{3\pi}{32 G \rho}}, \tag{6}$$

where G is the gravitational constant and ρ is the mean mass density. The mean free-fall time of the HMCC is calculated to be 1.16 ± 0.33 × 10^4 yr. This value is comparable with the lifetime of the HMCC.

Figure 13 plots the free-fall time derived from equation 6 vs. radius of the HMCCs and the dust cores; the former is $t_{\rm ff}/(yr) = 2.25 \times 10^4\ (r/(pc))^{0.42}$ and $2.51 \times 10^4\ (r/(pc))^{0.41}$ for $T_{\rm ex}$ = 50 K and 100 K, respectively, and the latter is $t_{\rm ff}/(yr) = 3.47 \times 10^4\ (r/(pc))^{0.20}$ and $4.87 \times 10^4\ (r/(pc))^{0.20}$ for $T_{\rm d}$=50 K and 100 K, respectively. The slope of the dust core is less steep than that of the HMCCs. The difference in the free-fall times must be due to the difference in the masses.

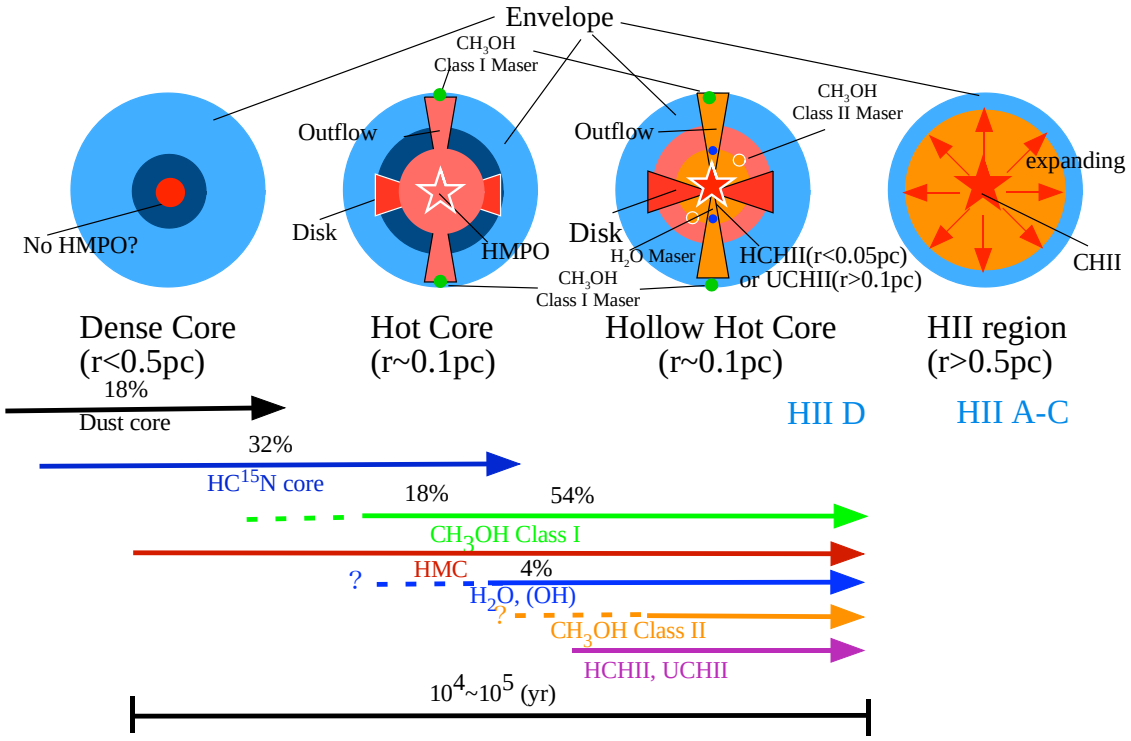

Fig. 10. Proposed evolutionary sequence in the 50 MC for the HMCs, $HC^{15}N$ cores, CH_3OH Class-I and Class-II masers, H_2O masers, OH masers, and HII regions. The "Dense Core" corresponds to the $HC^{15}N$ core. The evolutionary stages of the identified HMCs in our work include the "Dense Core", "hot core", and "Hollow Hot Core".

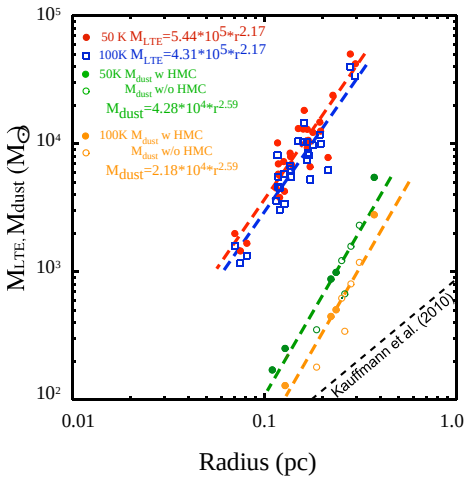

Fig. 11. Mass-size relation of the HMCCs. Red filled circles and blue open squares indicate the LTE masses calculated with T_{ex} = 50 K and 100 K, respectively. Green filled and open circles indicate the dust cores with T_d=50 K associated with a HMCC and no HMCC, respectively. Orange filled and open circles are the same as respective green circles except that the assumed temperature is T_d=100 K. Black dashed line shows the mass and size relation of cloud fragments in several molecular clouds over a wide range of radius 0.05 ≤ r ≤ 3 pc (Kauffmann et al. 2010a, 2010b).

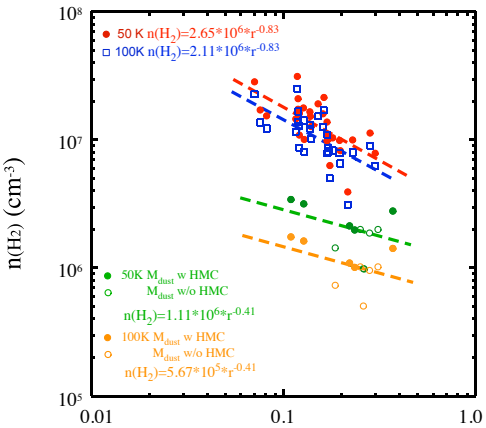

Fig. 12. Relation between the mean hydrogen number density and size of the HMCCs of our sample. The symbols and colors, as well as the assumed temperatures, are the same as those in Figure 11 except for the difference in the units of the vertical axis.

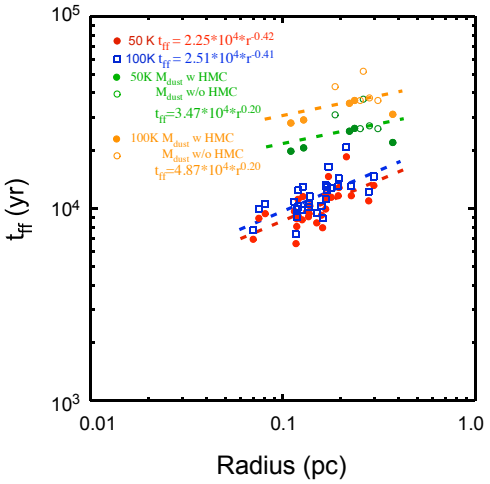

Fig. 13. Relation between the free-fall time and size of the HMCCs of our sample. The symbols and colors, as well as the assumed temperatures, are the same as those in Figure 11 except for the difference in the units of the vertical axis.

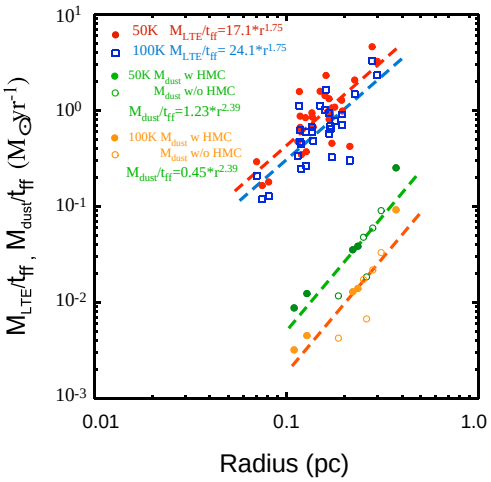

Fig. 14. Relation of the ratio of the LTE mass to the free fall time of the HMCCs and the dust cores against the radius. The symbols and colors, as well as the assumed temperatures, are the same as those in Figure 11 except for the difference in the units of the vertical axis.

Figure 14 shows the ratio of the LTE mass to the free fall time of the HMCCs and the dust cores as a function of the radius; the former is M_{LTE}/t_{ff} = 17.1 × (r/(pc))$^{1.75}$ and 24.1 × (r/(pc))$^{1.75}$ for T_{ex} = 50 K and 100 K, respectively, and the latter is M_{dust}/t_{ff} = 1.23 ×(r/(pc))$^{2.39}$ and 0.45 ×(r/(pc))$^{2.39}$ for T_d=50 K and 100 K, respectively. The mass accretion rate, $\dot{M}$, is calculated as

$$\dot{M}(M_\odot/yr) = f_{infall}\ \frac{M_{LTE}(M_\odot)}{t_{ff}(yr)}, \qquad (7)$$

where f_{infall} is the factor in v_{in}=f_{infall}×v_{ff} for the velocities of infall (v_{in}) and free-fall (v_{ff}). The value of f_{infall} was estimated to be 0.2–0.3 (Wyrowski et al. 2012). For r=0.1 pc, $\dot{M}$ reaches (6.1–9.1)× 10^{-2} $M_\odot yr^{-1}$ and (8.6–12.8) × 10^{-2} $M_\odot yr^{-1}$ for the HMCCs with T_{ex} = 50 K and 100 K, respectively. The mass accretion rate $\dot{M}$ is required to be at least 3 ×10^{-3} $M_\odot yr^{-1}$ to form massive stars (Fazal et al. 2008). A massive star has, in general, a Keplerian disk with Class-II CH_3OH masers (Beltrán & de Wit 2016). Sanna et al. (2019) showed that the accretion disk is truncated between 2000 and 3000 au, has a mass of about one-tenth of the central star mass, and is infalling toward the central star at a high rate of 6 ×10^{-1} $M_\odot yr^{-1}$. It is, however, unclear what kind of structure is inside the HMC at several thousands au and in the massive-protostar disc (Kratter & Matzner 2006; Goddi et al. 2011). At least, our estimated accretion rate is sufficient for massive star formation.

Figure 15 shows the scattered plot between the LTE mass and virial mass of the HMCCs: M_{virial} = 40.72 × $M_{LTE}^{0.58}$ and 46.24 × $M_{LTE}^{0.58}$ for the T_{ex} = 50 K and 100 K, respectively. The LTE masses of the HMCCs are almost proportional to the virial masses, as expected. Tsuboi et al. (2012) presented the LTE mass vs. virial mass relation of the molecular clumps in the 50 MC, showing the virial masses are about one order of magnitude smaller than the LTE masses for a similar mass range to that for the HMCCs of our samples. Miyazaki & Tsuboi (2000) showed the LTE masses of the molecular clumps in the CMZ are proportional to the virial masses with >10^4 $M_\odot$. Uehara et al. (2019) suggested that the molecular gas compression by the CCC efficiently formed the massive bound cores or massive cold cores with high masses of 2500–3000 $M_\odot$ or more. Our data points of the HMCCs at the bottom-left corner of Figure 15 are actually smoothly connected to the data points of the most massive cold cores presented by Uehara et al. (2019).

The scattered plot between the size and velocity dispersion of the HMCCs in the 50 MC is shown in Figure 16. A high degree of scatter is apparent in the plot, as quantitatively supported with the small correlation coefficient, indicating that the size and linewidth of the HMCCs are not correlated. However, Larson's first law (Larson 1981) shows power-law dependence of the velocity dispersion on the region size. We find that the data points of several HMCCs overlap with those of the cold cores (Uehara et al. 2019) and that the others have larger velocity widths than those of the cold cores. Therefore, the turbulence in the HMCs must be more active than that in the cold cores.

Although the outflow components are known to be significant at higher frequencies (van der Tak et al. 2003), these components are not significant in our observations. Therefore, the velocity width of the SO emission line means the turbulent velocity of the HMC itself. The results of turbulent velocities show a hierarchical structure for the molecular clump, cold core, and HMC (see, e.g., HMC05 and HMC27). If we adopt the hypothesis that cold cores coalesce in CCC and form a large-mass core, which is the parent body of a HMC, Figure 15

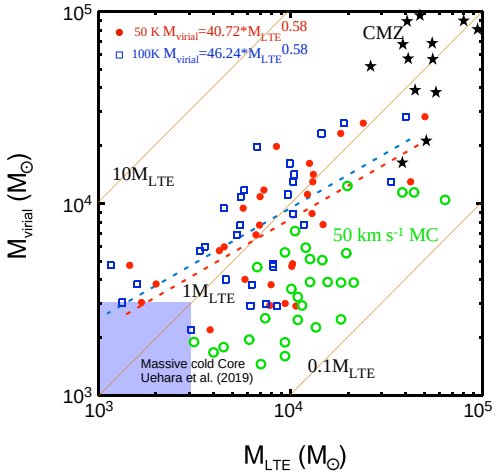

Fig. 15. Relation between the LTE mass and virial mass of the HMCCs of our sample for the assumed temperatures of T_{ex} = 50 K (in red filled circles) and 100 K (blue open squares). Orange lines show the relations M_{virial}=10 M_{LTE}, 1 M_{LTE}, and 0.1M_{LTE}. Green circles and asterisks indicate the results of the molecular clumps in the 50 MC (Tsuboi et al. 2012) and those in the CMZ (Miyazaki & Tsuboi 2000), respectively. Purple square at the bottom of the left corner indicates the range of the mass of massive cold cores (Uehara et al. 2019).

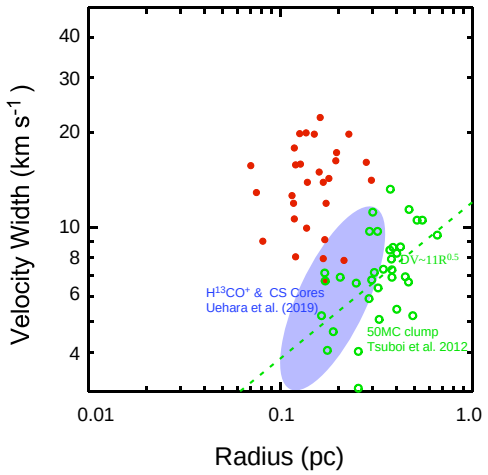

Fig. 16. Scattered plot of the velocity width vs. radius of the HMCCs of our sample. Red filled circles indicate the velocity widths of the HMCCs. Green circles indicate those of the molecular clumps in the 50 MC (Tsuboi et al. 2012). Purple oval near the bottom center shows the range of the velocity width-radius relation of cold cores derived from the $H^{13}CO^+$ and CS emissions (Uehara et al. 2019).

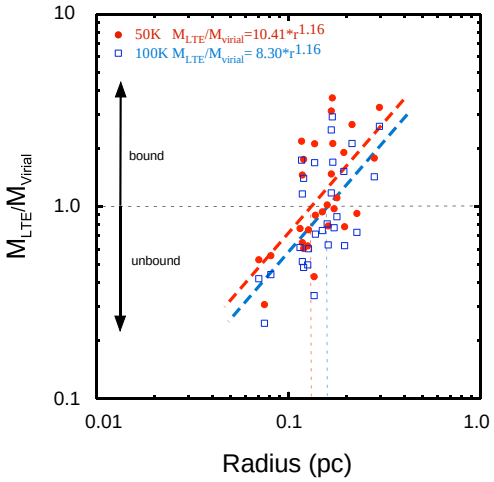

Fig. 17. Relation between the ratio of the virial to LTE masses and radius of the HMCCs of our sample. Red filled circles and blue open squares indicate the LTE masses calculated for T_{ex} = 50 K and 100 K, respectively.

and Figure 16 give indication about the coalescence process in which the radius does not change much while the velocity width and density increase. If a single large-mass core is formed, a HMPO should be formed due to the contraction of the core.

Figure 17 shows the relation between the ratio of the virial to LTE masses and radius of the HMCCs of our sample: $M_{LTE}/M_{virial} = 10.41 \times (r/(pc))^{1.16}$ and $8.30 \times (r/(pc))^{1.16}$ for T_{ex} = 50 K and 100 K, respectively. The ratio M_{LTE}/M_{virial} is 1.0 at radii of 0.13 pc and 0.16 pc for T_{ex} = 50 K and 100 K, respectively. Here, $M_{LTE}/M_{virial} > 1$ means gravitationally bound and <1, gravitationally unbound. In this case, the HMCCs with r < 0.1 pc are gravitationally unbound, whereas those with r > 0.1 pc are bound.

Figure 18 shows the relation between the velocity width and the ratio of the LTE to virial masses of HMCCs of our sample: $\Delta V_{FWHM} = 13.94 \times (M_{LTE}/M_{virial})^{0.29}$ and $13.04 \times (M_{LTE}/M_{virial})^{0.29}$ for T_{ex} = 50 K and 100 K, respectively. When M_{LTE}/M_{virial} = 1.0, ΔV_{FWHM} are 13.94 km s^{-1} and 13.04 km s^{-1}, respectively. These imply that the HMCCs with $\Delta V_{FWHM} < 13$ km s^{-1} are gravitationally bound, whereas those with $\Delta V_{FWHM} > 14$ km s^{-1} are gravitationally unbound. In the case of the velocity range, 13 km s^{-1} < ΔV_{FWHM} < 14 km s^{-1}, it depends on the temperature of HMCC, and it is unclear whether HMCC is gravitationally bound or unbound.

It is unclear whether the unbound regions in Figures 17 and 18 indicate the evolution of the HMC or characteristics of a small HMC with a small LTE mass. On the basis of star formation theories, however, if the surrounding material is accreting to the central HMSCs, dissipation by outflows will let the HMCs gravitationally unbound and their central density profiles will be flattened (e.g. Shu et al. 1987). Outflows with high mass-loss rates as well as radiation pressure and strong winds from the HMPOs or HCHIIs may accelerate the dissipation process.

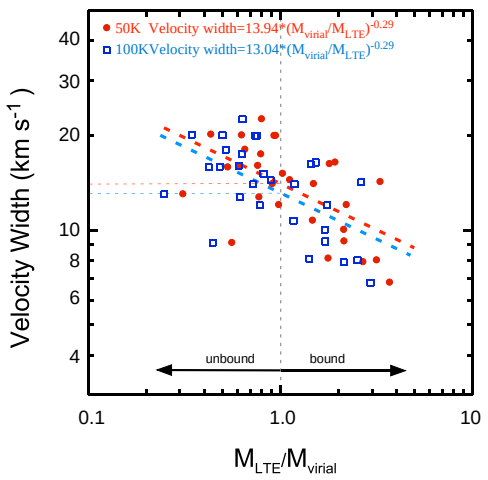

Fig. 18. Relation between the velocity width and the ratio of the LTE to virial mass of HMCCs of our sample. Red filled circles and blue open squares indicate the LTE masses calculated for T_{ex} = 50 K and 100 K, respectively.

Therefore, some of the HMCCs with a large velocity width in the 50 MC may evolve into the HMCs with HMPOs but without HCHIIs, yet.

4.3 Formation and Evolution of Massive Star in the 50 MC

In §4.1, we have concluded that most of the HMCCs in the 50 MC are in the early stages. In §4.2, some correlations have been presented between the HMCC radius, mass, density, mass accretion rate, etc. The overall inactive star formation in these CMZ clouds (see §1) may be a result of the strong turbulence in this region and/or clouds being still in the very early evolutionary stage where the collapse has only recently started (Lu et al. 2019a).

Formation of massive stars requires that molecular clumps with a moderate density ($\sim 10^{4-5}$ cm^{-3}) be compressed with some mechanism, such as CCC, supernova explosion, etc. In the 50 MC, CCC (e.g. Inoue & Fukui 2013; Fukui et al. 2020) is required efficiently to form massive and unstable cores as some simulation works show (e.g. Takahira et al. 2014, 2018). It would be reasonable to assume that a large amount of gas is compressed by not only gravity but some other factors triggered in r $\sim$ 0.1 pc before a HMC is formed, which is unstable and eventually collapses to form massive stars with a high mass-accretion rate. Indeed, observational indications of CCC having triggered gas compression have been reported with regard to massive star formation in the 50 MC (Tsuboi et al. 2011, 2015a, 2015b, 2019).

The timescale of the evolution of the HMC should depend on the mass of the HMC. Since the duration of the CCC is longer than the lifetime of the HMC as described below, we conjecture that the HMCs are formed and evolve in an order of 10^6 yr. Larger the mass is, faster the HMC evolves. When HMPOs are formed in the center of the HMC, the periphery of the HMC is left behind and eventually dissipates.

Uehara et al. (2017) identified 27 molecular-cloud filaments in the 50 MC. In addition, Uehara et al. (2019, 2021) examined whether the CS cores were influenced by CCC or not and argued that CCC efficiently formed massive bound cores even when the slope of the core mass function (often abbreviated as the CMF) was not greatly changed by CCC. Some massive CS cores produced by CCC may have evolved to the HMCCs that we observed. If so, the ages of the CS cores are probably (1–2) $\times$ 10^4 yr, which is comparable with those of HMCs01–28, HIIs-A, B, C, and D. In the 50 MC, the events of CCC are still ongoing in the 27 filaments (Uehara et al. 2017, 2021) with a duration timescale of $\sim 10^6$ yr. Then, we conjecture that the above-described three evolutionary stages of the HMC, i.e., dense core, hot core, and HHMC, take a combined timescale of 10^{4-5} yr.

A burst of star formation or a mini starburst may be taking place in the 50 MC region in a similar way as in Sgr B2 in the CMZ (e.g. Hasegawa et al. 1994; Sato et al. 2000), and W49A (e.g. Miyawaki et al. 2009) and W51A (e.g. Okumura et al. 2001) in the Galactic disk. In this case, it may be induced by CCC.

5 CONCLUSIONS

We present the results of 2.″5-resolution observations made with ALMA at 86 GHz in the continuum and SO ($N_J = 2_2 - 1_1$) emissions of the region of the Galactic Center Molecular Cloud G−0.02−0.07 (the 50 MC) in the CMZ.

1. The 86-GHz continuum emission, which mainly traces HII regions, found four HII regions of HII-A to D in the central part of the 50 MC.
2. No new UCHIIs, HCHIIs, or Class-II CH_3OH masers were detected.
3. Ten dust cores were identified in which five dust cores are positionally associated with HMCCs.
4. We identified 28 HMCCs around the HII regions, using "clumpfind" and visually inspecting the channel and integrated-intensity maps.
5. The masses of the identified dust cores and HMCCs were estimated under the LTE condition and they were found to be almost proportional to their virial masses. No correlation between the size and velocity width of the HMCCs, as expected in the Larson's first law, was found.
6. The relation between the ratio of the LTE to virial masses and radius shows that the HMCCs with radii r < 0.1 pc are bound, whereas those with r > 0.1 pc are unbound. We conclude that a contraction of the HMC ceases by the time the size has decreased to 0.1 pc, after which the size of the HMC

remains almost stable.

7. The HMCCs were likely to be formed through compression of molecular clumps triggered by external force, such as CCC and supernova explosion.
8. The HMCCs in the 50 MC are in an evolutionary stage of pre-HMC.

Acknowledgments

We thank the anonymous referee for their comments that helped us improve the manuscript considerably. We thank Dr. Yoshimi Kitamura for helpful discussions. This work is supported in part by the Grant-in-Aid from the Ministry of Education, Sports, Science and Technology (MEXT) of Japan, No.16K05308 and No.19K03939. The work presented in this paper makes use of the following ALMA data: ADS/JAO.ALMA #2012.1.00080.S. ALMA is a partnership of ESO (representing its member states), NSF (USA) and NINS (Japan), together with NRC (Canada), NSC and ASIAA (Taiwan), and KASI (Republic of Korea), in cooperation with the Republic of Chile. The Joint ALMA Observatory is operated by ESO, AUI/NRAO, and NAOJ. Data analysis was in part carried out on the open-use data analysis computer system at the Astronomy Data Center, ADC, of the NAOJ.

References

Akeson, R. L. & Carlstrom, J. E. 1996, ApJ, 470, 528

Amo-Baladrón, M. A., Martin-Pintado, J., & Martin, S. 2011, A&A, 526, A54

André P., Men'shchikov A., Bontemps S. et al. 2010, A&A, 518, L102

Bally, J., Rathborne, J. M., Longmore, S. N., Jackson, J. M., Alves, J. F., Bressert, E., Contreras, Y., Foster, J. B., Garay, G., Ginsburg, A., Johnston, K. G., Kruijssen, J. M. D., Testi, L., & Walsh, A. J.. 2014, ApJ, 795, 28

Battersby, C., Bally, J., & Svoboda, B. 2017, ApJ, 835, 263

Barnes, A. T.; Longmore, S. N.; Avison, A., Contreras, Y., Ginsburg, A., Henshaw, J. D., Rathborne, J. M., Walker, D. L., Alves, J., Bally, J., Battersby, C., Beltrán, M. T., Beuther, H., Garay, G., Gomez, L., Jackson, J., Kainulainen, J., Kruijssen, J. M. D., Lu, X., Mills, E. A. C., Ott, J., & Peters, T. 2019, MNRAS, 486, 283.

Beltrán, M. T. & de Wit, W. J. 2016, A&Arv, 24, 6

Berry, D. S. 2015, Astronomy & Computing, 10, 22

Beuther, H., Walsh, A., Schilke, P., Sridharan, T. K., Menten, K. M., & Wyrowski, F. 2002 A&A, 390, 289

Beuther, H., Churchwell, E., McKee, C., & Tan, J. 2007, in Protostars and Planets V, ed. B. Reipurth, D. Jewitt, & K. Keil (Tucson: University of Arizona Press), 165

Boonman, A. M. S., Stark, R., van der Tak, F. F. S., van Dishoeck, E. F., van der Wal, P. B., Schäfer, F., de Lange, G., & Laauwen, W. M. 2001, ApJ, 553, L63

Cotton, W. D., & Yusef-Zadeh, F. 2016, ApJS, 227, 10

Churchwell, E., Walmsley, C.M. & Cesaroni, R. 1990, A&AS 83, 119

Churchwell, E. 2002, ARA&A, 27

Coil, Alison L.; Ho, Paul T. P., 2000, ApJ, 533, 245

Cragg, D. M., Sobolev, A. M., & Godfrey, P. D. 2005, MNRAS, 360, 533

de la Fuente, E., Trinidad, M. A., Porras, A., Rodríguez-Rico, C., Araya, E. D., Kurtz, S., Hofner, P., & Nigoche-Netro, A. 2018, RMxAA, 54, 129

De Pree, C. G., Wilner, D. J., Goss, W. M., Welch, W. J., & McGrath, E. 2000, ApJ, 540, 308

De Pree, C. G., Wilner, D. J., Mercer, A. J., Davis, L. E., Goss, W. M., & Kurtz, S. 2004, ApJ, 600, 286

Ekers, R. D., van Gorkom, J. H., Schwarz, U. J., & Goss, W. M. 1983, A&A, 122, 143

Frail, D. A., Goss, W. M., Reynoso, E. M., et al. 1996, AJ, 111, 1651

Fazal, F. M., Sridharan, T. K., Qiu, K., Robitaille, T., Whitney, B., & Zhang, Q. 2008, ApJ, 688, L41

Fontani, F., Cesaroni, R., & Furuya, R. S., 2010, A&A, 517, 56

Fukui, Y.,Inoue, T., Hayakawa, T., & Torii K.. 2020, PASJ, in press

Furuya, R.S., Cesaroni, R., Takahashi, S., Momose, M., Testi, L., Shinnaga, H. & Codella, C. 2005, ApJ, 624, 827

Furuya, R.S., Cesaroni, R., & Shinnaga, H. 2011, A&A, 525, 72

Garay, G., & Lizano, S. 1999, PASP, 111, 1049

Goddi, C.; Greenhill, L. J.; Humphreys, E. M. L.; Chandler, C. J.; Matthews, L. D. 2011, ApJ, 739, 13

Goldsmith, P. F., & Langer, W. D. 1999, ApJ, 517, 209

Goss, W. M., Schwarz, U. J.;, van Gorkom, J. H.& Ekers, R. D., 1985, MNRAS, 215, 69

Hasegawa, T., Sato, F., Whiteoak, J. B., & Miyawaki, R. 1994, ApJ, 429, L77

Herbst, E. & van Dishoeck, E. F., 2009, ARA&A, 47, 427

Hildebrand, R. H. 1983, Quart, J. R. A. S., 24, 267

Ho, P. T. P., & Townes, C. H. 1983, ARA&A, 21, 239

Ikeda, M., Hirota, T., & Yamamoto, S., 2002, ApJ, 575, 250

Inoue,T., & Fukui, Y., 2013, ApJ, 774, L31

Jiménez-Serra, I., Zhang, Q., Viti, S., Martin-Pintado, J., & de Wit, W.-J. 2012, ApJ., 753, 34

Kauffman, M. J., Hollenbach, D. J., & Tielens, A. G. G. M. 1998, ApJ., 497, 276

Kauffmann, J., Pillai, T., Shetty, R., Myers, P. C., & Goodman, A. A. 2010a, ApJ., 712, 1137

Kauffmann, J., Pillai, T., Shetty, R., Myers, P. C., & Goodman, A. A. 2010b, ApJ., 716, 433

Kauffmann, J,.Pillai, T., Zhang, Q., Menten, K. M., Goldsmith, P. F., Lu, X., & Guzmán, A. E. 2017a, A&A, 603, A89;

Kauffmann, J,.Pillai, T., Zhang, Q., Menten, K. M., Goldsmith, P. F., Lu, X., & Guzmán, A. E. 2017b, A&A, 603, A90;

Kratter, K. M., & Matzner, C. D. 2006, MNRAS, 373, 1563

Kurtz, S., Cesaroni, R., Churchwell, E., Hofner, P., & Walmsley, C. M. 2000, in Protostars and Planets IV, eds Mannings, V., Boss, A.P., Russell, S. S. (Tucson: University of Arizona Press), 299

Larson, R. B. 1981, MNRAS, 194, 809

Li, J., Wang, J., Zhu, Q., Zhang, J., & Li, D. 2015, ApJ, 802, 40

Li, C., Wang, H., Wu, Y., Ma, Y., & Lin, Li. 2020, RAA, 20, 31

Lu, X., Zhang, Q. Kauffmann, J.,Pillai, T., Ginsburg, A., Mills, E. A. C., Kruijssen, J. M. D., Longmore, S. N., Battersby, C., Liu, H. B., & Gu, Q., 2019a, ApJ, 872, 171

Lu, X., Mills, E. A. C., Ginsburg, A., Walker, D. L., Barnes, A. T., Butterfield, N. Henshaw, J. D., Battersby, C., Kruijssen, J. M. D., Longmore, S. N., Zhang, Q.,Bally, J., Kauffmann, J. Ott, J., Rickert, M., & Wang, K. 2019b, ApJ Suppl, 244, 35

McEwen, B. C., Sjouwerman, L. O.& Pihlstr\`om, Y. M. 2016, ApJ, 832, 129

Mac Low, M-M, Toraskar, J., Oishi, J. S., & Abel, T. 2007, ApJ, 688, 980

McMullin, J. P., Waters, B., Schiebel, D., Young, W., & Golap, K. 2007, Astronomical Data Analysis Software and Systems XVI (ASP Conf.

Ser. 376), ed. R. A. Shaw, F. Hill, & D. J. Bell (San Francisco, CA: ASP), 127
Mills, E. J., Goss, W. M., & De Pree, C. G. 2011 ApJ, 735, 84
Minier, V., Burton, M. G., Hill, T., Pestalozzi, M. R., Purcell, C., Garay, G., Walsh, A., & Longmore, S., 2005, A&A, 429, 945
Miyawaki, R., Hasegawa, T., & Hayashi, M. 2002, The Proceedings of the IAU 8th Asian-Pacific Regional Meeting (the Astronomical Society of Japan, Tokyo) 171
Miyawaki, R., Hayashi, M., & Hasegawa, T., 2009, PASJ, 61, 39
Miyazaki, A. & Tsuboi, M. 2000, ApJ, 536, 357
Motte, F., Bontemps, S., & Louvet, F. 2018, ARA & A, 56, 41
Morris, M., & Serabyn, E., 1996, ARA & A, 34, 645
Nomura, H. & Millar, T. J.. 2004, A&A, 414, 409
Okumura, S., Miyawaki, R., Sorai, K., Yamashita, T., & Hasegawa, T. 2001, PASJ, 53, 793
Pestalozzi, M., Humphreys, E. M. L., & Booth, R. S., 2002, A&A, 384, L15
Phillips, C. J., Norris, R. P., Ellingsen, S. P., & McCulloch, P. M. 1998, MNRAS, 300, 1131
Pihlstrröm, Y. M., Sjouwerman, L. O., & Mesler, R. A. 2011, ApJ, 740, 66
Pineda, J. E., Rosolowsky, Erik W., & Goodman, A. A. 2009, ApJ, 699, L134
Pillai, T., Kauffmann, J., Tan, J. C., et al. 2015, ApJ, 799, 74
Plambeck, R. L., Wright, M. C. H., Welch, W. J., Bieging, J. H., Baud, B., Ho, P. T. P., & Vogel, S. N. 1982, ApJ, 259, 617
Rathborne, J. M., Longmore, S. N., Jackson, J. M., Kruijssen, J. M. D., Alves, J. F., Bally, J., Bastian, N., Contreras, Y., Foster, J. B., Garay, G., Testi, L., & Walsh, A. J 2014, ApJ, 795, L25
Rathborne, J. M., Longmore, S. N., Jackson, J. M., Alves, J. F., Bally, J., Bastian, N., Contreras, Y., Foster, J. B., Garay, G., Kruijssen, J. M. D., Testi, L., & Walsh, A. J. 2015, ApJ, 802, 125
Rolffs, R., Schilke, P., Zhang, Q., & Zapata, L. 2011, A&A, 536, 33
Rosolowsky, E. W., Pineda, J. E., Kauffmann, J., & Goodman, A. A. 2008, ApJ, 679, 1338
Sanna, A., Cesaroni, R., Moscadelli, L., Zhang, Q., Menten, K. M., Molinari, S., Caratti, A., o Garatti, A., & De Buizer, J. M. 2014, A&A, 565, 34
Sanna, A., Kölligan, A., Moscadelli, L, Kuiper, R., Cesaroni, R., Pillai, T., Menten, K. M., Zhang, Q., Caratti o Garatti, A., Goddi, A., Leurini, S., & Carrasco-González, C. 2019, A&A, 623, 77
Sato, F., Hasegawa, T., Whiteoak, J. B., & Miyawaki, R. 2000, ApJ, 535, 857
Sewilo, M., Churchwell, E., Kurtz, S., Goss, W. M. & Hofner, P. 2004, ApJ, 609, 285
Sewilo, M., Churchwell, E., Kurtz, S., Goss, W. M. & Hofner, P. 2011, ApJS, 194, 44
Schilke, P., Benford, D. J., Hunter, T. R., Lis, D. C., & Phillips, T. G. 2001, ApJS, 132, 281
Shu, F. H., Adams, F. C., & Lizano, S. 1987, ARA&A, 25, 23
Silva, A., , Zhang, Q., Sanhueza, P., Lu, X., Beltrán, M. T., Fallscheer, C., Beuther, H., Sridharan, T. K., & Cesaroni, R., 2017, ApJ, 847, 87
Sjouwerman, L. O., & Pihlstrröm, Y. M., 2008, ApJ, 681, 1287
Sridharan, T. K., Beuther, H., Schilke, P., Menten, K. M., & Wyrowski, F. 2002, ApJ, .566, 931
Stéphan, G., S., Schilke, P., Le Bourlot, J., Schmiedeke, A., Choudhury, R., Godard, B., & Sánchez-Monge, Á. 2018, A&A, 617, 60
Stutzki, J., & Guseten, R. 1990, ApJ, 356, 513
Takahira, K., Tasker, E. J., & Habe, A., 2014, ApJ, 792, 63
Takahira, K., Shima, K, Habe, A., & Tasker, E. J. 2018, PASJ, 70, 1
Takekawa, S., Oka, T., & Tanaka, K. 2017a, ApJ, 834, 121
Takekawa, S., Oka, T., Iwata, Y., Tokuyama, S., & Nomura, M. 2017b, ApJ, 843, L11
Tanaka, K. E. I. , Tan, J. C., Zhang, Y. 2016, ApJ, 818, 52
Tsuboi, M., Miyazaki, A., & Okumura, S., 2009, PASJ, 61, 29
Tsuboi, M., Tadaki, K., Miyazaki, A., & Handa, T. 2011, PASJ, 63, 763
Tsuboi, M., & Miyazaki, A., 2012, PASJ, 64, 111
Tsuboi, M., Miyazaki, A., & Uehara, K. 2015a, PASJ, 67, 90
Tsuboi, M., Miyazaki, A., & Uehara, K. 2015b, PASJ, 67, 109
Tsuboi, M., Kitamura,, Y., Uehara, K., Miyazaki, A., Miyawaki, R., Tsutsumi, T., & Miyoshi, M. 2019, PASJ, 71, 128
Tsuboi, M., Kitamura,, Y., Uehara, K., Miyawaki, R., Tsutsumi, T.,& Miyazaki, A. 2021, PASJ, 73, S91
Uehara, K., Tsuboi, M., Kitamura, Y., Miyawaki, R., & Miyazaki, A. 2017, in The Multi-Messenger Astrophysics of the Galactic Centre, Proceedings of the International Astronomical Union, IAU Symposium, 322, pp.162
Uehara, K., Tsuboi, M., Kitamura, Y., Miyawaki, R., & Miyazaki, A. 2019, ApJ, 872, 121
Uehara, K., Tsuboi, M., Kitamura, Y., Miyawaki, R., & Miyazaki, A. 2021 to be submitted
van der Tak, F. F. S., Boonman, A. M. S., Braakman, R., & van Dishoeck, E. F. 2003, A&A, 412, 133.
van der Tak, F.F.S., Black, J.H., Schöier, F.L., Jansen, D.J., van Dishoeck, E.F. 2007, A&A, 468, 627
Walker, D. L., Longmore, S. N., Zhang, Q., Battersby, C.; Keto, E., Kruijssen, J. M. D., Ginsburg, A., Lu, X., Henshaw, J. D., Kauffmann, J., Pillai, T., Mills, E. A. C., Walsh, A. J., Bally, J., Ho, L. C., Immer, K., & Johnston, K. G. 2018, MNRAS, 474, 2373
Walsh, A.J., Burton, M.G., Hyland, A.R. & Robinson, G. 1998, MNRAS, 301, 640
Walsh, A. J., Macdonald, G. H., Alvey, N. D. S., Burton, M. G., & Lee, J.-K., 2003, A&A, 410, 597
Williams, J. P., de Geus, E. J., & Blitz, L. 1994, ApJ, 428, 693
Wilner, D. J., De Pree, C. G., Welch, W. J., & Goss, W. M. 2001, ApJ, 550, L81
Wright, M. C. H., Plambeck, R. L., & Wilner, D. J. 1996, ApJ, 469, 216
Wyrowski, F., Güsten, R., Menten, K. M., Wiesemeyer, H. &Klein, B. 2012 A&A, 542, 2012
Yusef-Zadeh, F., Lacy, J. H., Wardle, M., Whitney, B., Bushouse, H., Roberts, D. A., & Arendt, R. G. 2010, ApJ, 725, 1429
Yusef-Zadeh, F., Cotton, W., Viti, S., Wandle, M., & Royster, M. J. 2013, ApJL, 452, L19
Zinchenko, I., & Henkel, C. 2017, in Proceedings of the IAU Symposium No. 332 , Astrochemistry VII - Through the Cosmos from Galaxies to Planets, 274